

Generative AI for Rapid Diffusion MRI with Improved Image Quality, Reliability and Generalizability

Amir Sadikov¹², Xinlei Pan³, Hannah Choi¹, Lanya T. Cai¹, and Pratik Mukherjee¹²

¹ Radiology and Biomedical Imaging, University of California, San Francisco

² Graduate Group in Bioengineering, University of California, San Francisco

³ University of California, Berkeley

amir.sadikov@ucsf.edu

Abstract

Background Diffusion MRI (dMRI) is a non-invasive, in-vivo biomedical imaging method for mapping tissue microstructure. Applications include structural connectivity imaging of the human brain, as well as detecting microstructural neural changes not detectable by other clinical neuroimaging techniques. However, acquiring high signal-to-noise ratio (SNR) dMRI datasets with high angular and spatial resolution requires prohibitively long scan times, limiting usage in many important clinical settings, especially for children, the elderly, and in acute neurological disorders that may require conscious sedation or general anesthesia. **Methods** We employ a Swin UNET Transformers (Swin UNETR) model, trained on augmented Human Connectome Project (HCP) data and conditioned on registered T1 scans, to perform generalized denoising of dMRI. We also qualitatively demonstrate super-resolution with artificially downsampled HCP data in normal adult volunteers.

Results Remarkably, Swin UNETR can be fine-tuned for an out-of-domain dataset with a single example scan, as we demonstrate on dMRI of children with neurodevelopmental disorders and of adults with acute evolving traumatic brain injury, each cohort scanned on different models of scanners with different dMRI imaging protocols at different sites. This robustness to scan acquisition parameters, patient populations, scanner types, and sites eliminates the advantages of self-supervised machine learning methods over our fully supervised generative AI approach. We exceed current state-of-the-art denoising methods in accuracy and test-retest reliability of rapid diffusion tensor imaging (DTI) requiring only 90 seconds of scan time. Applied to tissue microstructural modeling of dMRI at high diffusion-weighting and therefore low SNR, Swin UNETR denoising achieves dramatic improvements over the state-of-the-art for test-retest reliability of intracellular volume fraction and free water fraction measurements and is able to remove heavy-tail noise, improving biophysical modeling fidelity. **Conclusion** Swin UNETR enables rapid diffusion MRI with unprecedented accuracy and reliability, especially at high diffusion-weighting for probing biological tissues at microscopic spatial scales for scientific and clinical applications.

The code and model are publicly available at <https://github.com/ucsfnc1/dmri-swin>.

1 Introduction

Diffusion MRI (dMRI) can provide valuable clinical information and assess tissue microstructure; however, its low signal-to-noise (SNR) ratio can result in poor diagnostic and quantitative accuracy [6]. To improve SNR, most dMRI protocols require low angular and spatial resolution or a long scan time, which limits usage in many important clinical settings. Therefore, there is great interest in having short patient scan times without compromising SNR or spatial and angular resolution.

Several supervised methods have been proposed to denoise brain dMRI scans; however, they are limited by their lack of generalizability. Often, they work on only one b-value and a prespecified set of diffusion-encoding directions, are built to predict only one set of microstructural parameters, or are trained and validated on the same dataset, such as the Human Connectome Project (HCP) [27][15]. Diffusion data can vary widely due to different acquisition parameters, scanners, and patient populations and therefore unsupervised or self-supervised denoising methods are often preferred [10]. However, these self-supervised and unsupervised methods do not approach the performance of supervised techniques on data within the trained domain and can still perform variably with different out-of-domain datasets.

In addition, most dMRI denoising methods are evaluated only qualitatively or by denoising a subset of the data and evaluating the accuracy with respect to the full dataset. In this paper, we also evaluate denoising using external validation via test-retest reliability for Diffusion Tensor Imaging (DTI) [22] and Neurite Orientation Dispersion and Density Imaging (NODDI) [31] metrics to ensure precision as well as via known Structural Covariance Networks (SCNs) [30][16] derived from those metrics in the white matter (WM) and gray matter (GM) to ensure biological accuracy. Finally, we pay special attention to the ability to remove heavy-tail noise, which can lead to biased biophysical metrics from fitting algorithms primarily designed for data corrupted with Gaussian noise.

Here we propose to use a Swin UNETR (Swin UNETR) model [12] to denoise dMRI data conditioned on registered T1 scans. Unlike other supervised methods, which utilize a small subset of the HCP dataset (typically 40 subjects) for training [27][15], we use the full set of HCP data, training with all b-values and diffusion-encoding directions, and apply simple data augmentations, such as random flipping, rotation, scaling, and k-space downsampling. Training on a large dataset, close to 300,000 3D volumes across 1021 subjects, allows the Swin UNETR model to learn a denoising function that generalizes well to many different conditions. In addition to the Swin UNETR, we also train a UNet convolutional neural network model that lacks a transformer component to determine the effect, if any, of network architecture on denoising performance. We validate our approach on a held-out HCP Retest dataset as well as three ex-

ternal datasets acquired in different patient populations using different scanners and dMRI protocols, showing significant benefits over current state-of-the-art self-supervised and unsupervised methods. In addition to improvements in accuracy, we also show better repeatability on the HCP Retest dataset. Finally, we demonstrate that fine-tuning, even on only one subject, improves performance on out-of-domain datasets and that our approach can also super-resolve dMRI data via qualitative assessment in an HCP subject.

2 Methods

2.1 Data

In our experiments, we used data from four different datasets the first of which comprising normal young adult volunteers is separated into a training dataset and a held-out dataset within this same training domain. The other three datasets are out-of-domain (OOD) patient research datasets for establishing generalizability and clinical applicability.

- **HCP:** 1021 subjects from the Human Connectome Project (HCP) Young Adult dataset [9] acquired using 90 diffusion-encoding directions at b-values of $b=1000, 2000, 3000 \text{ s/mm}^2$ with 1.25 mm resolution. We used all 1021 subjects for training and excluded any subjects in the HCP Retest dataset.
- **HCP Retest:** 44 subjects from the HCP Retest dataset used for validating denoising performance and repeatability. It was acquired in the same way as the HCP dataset.
- **TBI:** 45 adult mild traumatic brain injury patients acquired two decades ago using protocols identical to [30] on a 3T GE scanner with 55 diffusion-encoding directions at $b=1000 \text{ s/mm}^2$ with a nominal resolution of 1.8 mm (0.9 mm in xy after zero-interpolation in k-space). We randomly selected 5 subjects for fine-tuning and 40 subjects for testing.
- **SPIN:** 45 children ages 8-12 years with neurodevelopmental disorders acquired on a 3T Siemens Prisma scanner with 64 and 96 diffusion-encoding directions at b-values of $b = 1000, 2500 \text{ s/mm}^2$ respectively (TE=72.20 ms, TR=2420 ms, flip angle=85°) with 2.00 mm isotropic resolution. We randomly selected 5 subjects for fine-tuning and 40 subjects for testing.
- **AHA:** 8 children and adolescents ages 8 - 18 with intracerebral hemorrhage due to vascular malformations, primarily arteriovenous malformations (AVMs), undergoing resection acquired on a 3T GE MR750 with 55 diffusion-encoding directions at $b=2000 \text{ s/mm}^2$ with a resolution of 2.00 mm that was zero-interpolated in-plane to 1.00 x 1.00 mm. Data was collected over three sessions: first, prior to resection, the second, six months after surgery, and the third, one year following surgery. Lesion location was determined by radiology notes. We selected a ninth subject for fine-tuning and had a total of 23 sessions for testing (one subject had only two sessions).

DMRI data was skull-stripped with Synthstrip [13], corrected for eddy current-induced distortions and subject movements with Eddy [1], and aligned to structural 3D T1 scans with Boundary-Based Registration [11]. T1 scans were also skull-stripped using Synthstrip and segmented using SynthSeg [2]. For the AHA dataset, due to the hemorrhagic lesion impacting SynthSeg performance, T1 scans were instead segmented using Freesurfer’s recon-all command with the SynthSeg option enabled and, in a few cases where recon-all failed, the recon-all-clinical command was used instead. Finally, co-registered T1 and dMRI scans were resampled with 5th order spline interpolation at 1.25 mm and used as inputs to the model.

2.2 Denoising Validation

To evaluate the denoising algorithms and possible scan time speedup, we measure performance in both fully-sampled and subsampled data. We chose the minimum number of diffusion gradients necessary for unique fits: 6 for DTI, 15 for 4th order spherical harmonic, and 28 for 6th order spherical harmonic along with 1 $b=0$ s/mm² volume. We select the directions to minimize the condition number of the design matrix using the procedure described in [28][25]. For NODDI estimation, we only use the fully-sampled HCP acquisition. We compare the performance of the SWIN UNeTR and UNet models with three state-of-the-art unsupervised/self-supervised machine learning methods for dMRI denoising: block-matching and 4D filtering (BM4D) [20], Marchenko-Pastur Principal Component Analysis (MPPCA) [29], and Patch2Self (P2S) [10].

To evaluate DTI estimation, the mean absolute error (MAE) between the ground truth fully-sampled dataset and the model predictions in the subsampled dataset for the principal eigenvector (V1), fractional anisotropy (FA), axial diffusivity (AD), radial diffusivity (RD), and mean diffusivity (MD) were found. For evaluating higher order spherical harmonics, the Jensen–Shannon distance (JSD) between the ground truth and model predictions, projected onto a uniformly distributed 362 direction hemisphere, was used [4]. In each case, the ground truth was found by fitting the model using all acquired diffusion gradient directions. These errors were reported for WM and GM. DTI estimation was only conducted on the lowest shell ($b=1000$ s/mm²) for multi-shell datasets, whereas spherical harmonic estimation was conducted on every shell. To evaluate super-resolution performance, dMRI data from an HCP subject was k-space downsampled by a factor of two and then upsampled to emulate a low resolution acquisition.

We explore denoising in an (OOD) dataset for clinical translation by applying our model on the AHA dataset, which consists of children with intracerebral hemorrhage undergoing lesion resection scanned before and after intervention. We collect global WM and GM DTI metrics and measure perilesional changes in DTI microstructure over time from both subsampled and fully-sampled shells. To investigate the output distribution and effect of signal rectification, we measure the signal in the lateral ventricles, a region which consists almost solely of free water and has a heavily-attenuated uniform signal, across all diffusion-encoding

directions and compare the resulting signal intensity histograms produced by the denoising methods.

Microstructural repeatability was assessed using the HCP Retest dataset by measuring the within-subject coefficient of variation (CoV) for DTI and NODDI parameters across the two sessions. Briefly, we consider DTI test-retest reliability performance on both the fully-sampled and subsampled $b=1000 \text{ s/mm}^2$ shell. For NODDI estimation, we consider the full multi-shell HCP acquisition. To evaluate repeatability in WM regions, we conduct tract-based spatial statistics (TBSS) analysis via FA registration to a template using the Johns Hopkins University (JHU) atlas [26].

We also investigate the repeatability of SCNs by measuring the mean absolute difference between SCNs derived from the first and second sessions. We quantify both GM SCNs, which encompass only cortical GM regions from the Desikan-Killiany-Tourville atlas, and WM SCNs, which encompass only the JHU WM tracts given by TBSS analysis. We evaluate performance for DTI SCN repeatability on the subsampled $b=1000 \text{ s/mm}^2$ shell and for NODDI SCN repeatability on the fully-sampled acquisition using all shells. Finally, we also compute the MAE between the denoised subsampled DTI SCNs and the ground truth DTI SCN, computed by collecting the average DTI values for each region across both sessions using the fully-sampled $b=1000 \text{ s/mm}^2$ shell.

2.3 Training and Implementation

The Swin UNETR model [12][17] is implemented using PyTorch [23] and MONAI [3] (Fig. S5). The model was trained on a NVIDIA V100 GPU using mean-squared error loss between the model output and ground truth. To obtain ground truth dMRI data for training, a 6th order spherical harmonic was fit for each shell and projected onto the acquired directions. We chose AdamW [18] as an optimizer with a learning rate of 1e-5 and train using gradient clipping with a maximal norm of 1.0 and 16-bit precision for 14 epochs of training. During training, we first downsample the dMRI scan with a probability of 0.5 in frequency space to an anisotropic resolution between 1.25 and 3 mm and linearly upsample back to 1.25 mm resolution [19]. Random patches of 128 x 128 x 128 are cropped from the scan and randomly flipped with a probability of 0.5 along all axes and randomly rotated by 0, 90, 180, or 270 degrees along all axes with equal probability. The input dMRI patch is normalized to have zero mean and unit variance and the input T1 patch is normalized to have zero mean and standard deviation uniformly log-scaled between 0.25 and 4.0. For inference, we use a sliding window approach with an overlap of 0.875 and use 5th order spline interpolation to upsample the data. Fine-tuning was achieved via additional training on external data from one held-out subject out of five with a learning rate of 1e-6 for three epochs and the average result for validation was reported. Finally, since our models are trained and evaluated on the HCP dataset with 1.25 mm resolution, model predictions are resampled to native dMRI resolution for external OOD dataset validation. UNet model training, fine-tuning, and validation was

conducted in the same way, except training was extended to 20 epochs. Training for both the Swin and UNet models continued until training loss stabilized.

3 Results

3.1 Denoising Performance

For DTI estimation, the Swin model achieves the lowest MAE in all metrics in WM and GM in the HCP and TBI validation datasets, even without any fine-tuning (Table 1). For the SPIN dataset, the Swin model also outperforms all other models, except for FA estimation in GM where BM4D achieved the best result. In the AHA dataset, with the exception of MD and RD, the Swin model achieves lower MAE than any other method. While the UNet performs better than BM4D, MPPCA, and P2S in most settings, its performance still lags behind the Swin model, especially the fine-tuned Swin model. Patch2Self performs worse than the other denoising methods in this setting, especially for V1 estimation. Qualitative comparisons are consistent with these quantitative results and show that the Swin model is able to capture more of the finer features in the WM and GM microstructure without the excessive smoothing of BM4D and MPPCA (Supplementary Figs. S1, S2, S3, S4).

Finally, we examine the noise distribution of each denoising algorithm in the lateral ventricles of one subject from the AHA dataset (Fig. 1B). Unlike the other denoising algorithms, the Swin model is able to transform the original data distribution, a heavy-tailed Rician-like distribution, into a more Gaussian-like distribution with significantly smaller variance and skew but greater kurtosis.

3.2 Test-Retest Reliability

The Swin model achieves the lowest CoV between the test and retest datasets for all metrics in GM and AD and MD in WM using the 6-direction subsampled shell as well as MD and RD in both GM and WM for the 90-direction fully-sampled shell (Table 2). When using 90 directions, applying no denoising leads to the lowest CoV for AD and MPPCA achieves the best result for FA estimation.

For repeatability of intracellular volume fraction (ICVF), fiber orientation dispersion index (ODI), and free water fraction (ISOVF), where all acquired data was used, Swin outperforms all other denoising methods except for ODI estimation in GM, where P2S is slightly better. In particular, Swin excels at ICVF repeatability, achieving close to 50 % lower CoV than the next best method on average and achieves dramatically lower CoV on regional GM and WM measurements (Fig. 1A). Swin also achieves considerably better test-retest reliability than the other denoising approaches for ISOVF as well, especially in global and regional GM measurements (Fig. 1A).

Swin generates the most accurate FA, MD, and RD SCN in WM and FA and RD SCN in GM. Patch2Self achieves the lowest error for AD and MD SCN in GM, while MPPCA has the most accurate AD SCN in WM. MPPCA achieves

Table 1. MAE of FA, MD, RD, AD, and V1 estimation using six-direction HCP, SPIN, TBI, and AHA data in white matter (WM) and gray matter (GM) via no denoising (RAW), P2S, MPPCA, BM4D, UNET, SWIN with no fine-tuning (SWIN), UNET with fine-tuning on one subject (UNET-F1), and SWIN with fine-tuning on one subject (SWIN-F1). Best results are **bolded**.

Dataset	Tissue	Metric	RAW	P2S	MPPCA	BM4D	UNET	UNET-F1	SWIN	SWIN-F1
HCP	WM	AD	0.13	0.285	0.101	0.0848	0.0913		0.0811	
		FA	0.0935	0.249	0.0672	0.0563	0.0556		0.0496	
		MD	0.0657	0.0695	0.0556	0.0483	0.0526		0.0452	
		RD	0.0773	0.124	0.0622	0.0541	0.0558		0.0488	
		V1	19.7	66.9	15.2	13.9	13.4		12.6	
	GM	AD	0.133	0.107	0.0903	0.0931	0.0957		0.0794	
		FA	0.111	0.0793	0.0542	0.0588	0.0569		0.0484	
		MD	0.0723	0.0728	0.07	0.0683	0.0725		0.0597	
		RD	0.0849	0.0814	0.0731	0.0719	0.0754		0.0626	
		V1	33.6	64.1	28.7	28.1	28.4		26.7	
TBI	WM	AD	0.211	0.295	0.173	0.206	0.133	0.14	0.131	0.13
		FA	0.145	0.229	0.117	0.14	0.0866	0.0864	0.0922	0.0808
		MD	0.0941	0.0966	0.0886	0.0907	0.0743	0.0784	0.073	0.0702
		RD	0.116	0.138	0.103	0.111	0.0841	0.0848	0.085	0.076
		V1	26.6	67.1	24.2	26.1	21.5	21.8	22.1	21.0
	GM	AD	0.218	0.136	0.173	0.217	0.147	0.151	0.149	0.127
		FA	0.181	0.0966	0.139	0.175	0.102	0.102	0.123	0.0949
		MD	0.0908	0.0897	0.089	0.0893	0.0905	0.0926	0.0809	0.0817
		RD	0.124	0.0982	0.11	0.12	0.102	0.104	0.102	0.0948
		V1	38.0	62.0	36.6	37.6	35.5	35.6	36.2	35.0
SPIN	WM	AD	0.112	0.594	0.099	0.0999	0.0869	0.0844	0.0825	0.0767
		FA	0.0829	0.178	0.0768	0.0747	0.0609	0.0578	0.057	0.0518
		MD	0.0553	0.203	0.0446	0.0438	0.0491	0.0415	0.044	0.0402
		RD	0.0657	0.128	0.0561	0.0536	0.056	0.0479	0.0504	0.0457
		V1	18.4	63.9	16.9	15.0	14.8	14.6	14.5	13.8
	GM	AD	0.106	0.652	0.0759	0.0823	0.0905	0.0746	0.0859	0.0694
		FA	0.0994	0.193	0.0571	0.0508	0.0617	0.0559	0.0636	0.0517
		MD	0.0527	0.207	0.0506	0.0652	0.0611	0.0494	0.056	0.0471
		RD	0.066	0.106	0.057	0.0703	0.0642	0.0555	0.0609	0.0529
		V1	30.9	59.7	30.5	28.8	28.3	27.8	28.3	26.9
AHA	WM	AD	0.145	0.337	0.0981	0.14	0.091	0.0987	0.088	0.0921
		FA	0.0824	0.225	0.0661	0.0796	0.06	0.0736	0.0607	0.0591
		MD	0.0407	0.15	0.0312	0.0389	0.0378	0.0396	0.0371	0.0362
		RD	0.0489	0.189	0.0378	0.0466	0.041	0.0502	0.0414	0.0374
		V1	20.1	69.2	18.1	19.4	16.6	16.8	17.2	16.0
	GM	AD	0.173	0.462	0.101	0.161	0.0866	0.0917	0.0943	0.0801
		FA	0.0988	0.107	0.0685	0.0947	0.0569	0.0577	0.0721	0.0535
		MD	0.0484	0.247	0.0375	0.0449	0.047	0.057	0.0445	0.0441
		RD	0.0611	0.183	0.0454	0.0574	0.0497	0.0588	0.0516	0.0464
		V1	31.1	64.7	29.4	30.5	28.5	28.3	29.7	27.7

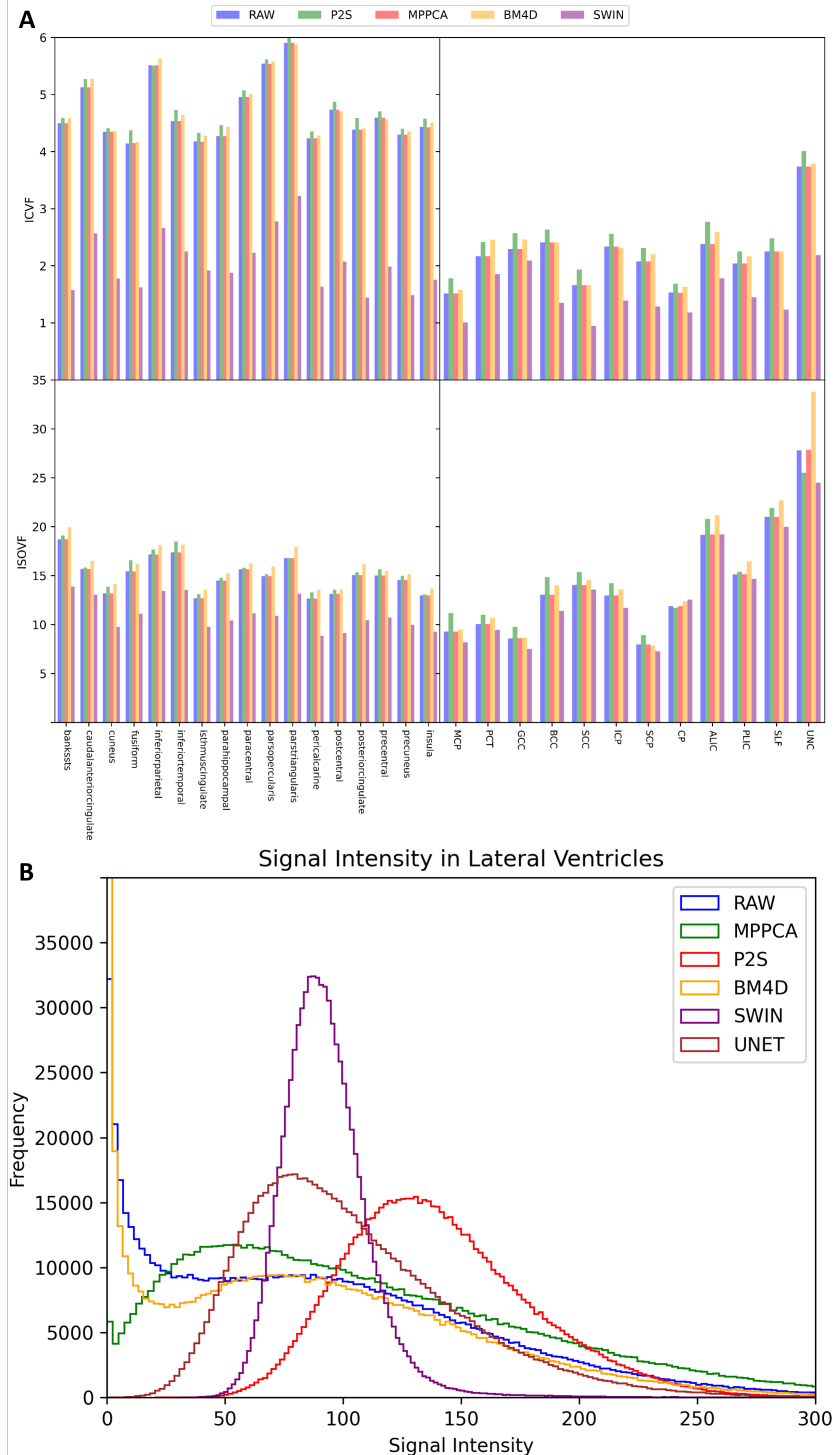


Fig. 1. (A) ICVF and ISOVF CoV (%) in select WM and GM regions and (B) histogram of signal intensity in the $b=2000$ s/mm^2 shell in the lateral ventricles of an AHA patient. Results using no denoising (RAW), P2S, BM4D, MPPCA, SWIN, and UNET denoising are displayed.

Table 2. Average CoV (%) across all WM and GM regions for DTI estimation using 6 and 90 direction subsets of the B1000 shell and NODDI estimation using all available data. The MAE for DTI SCN estimation using 6 direction subsets and the repeatability error for DTI and NODDI SCNs using all available data. Results using no denoising (RAW), P2S, BM4D, MPPCA, and SWIN denoising are displayed. Best results are **bolded**.

Validation	Tissue	Metric	RAW	P2S	MPPCA	BM4D	SWIN
6-Direction DTI CoV	WM	AD	2.438	3.02	2.526	2.43	2.339
		FA	2.603	7.492	3.09	2.912	2.922
		MD	2.986	3.429	3.014	2.987	2.901
		RD	5.273	4.009	5.136	5.123	4.846
	GM	AD	2.447	2.451	2.54	2.436	2.295
		FA	4.365	5.782	6.267	4.5	4.186
		MD	2.518	2.529	2.536	2.524	2.436
		RD	2.788	2.615	2.73	2.715	2.611
90-Direction DTI CoV	WM	AD	1.541	1.668	1.544	1.573	1.592
		FA	2.484	2.527	2.432	2.851	3.005
		MD	1.573	1.702	1.577	1.562	1.553
		RD	1.649	1.772	1.653	1.617	1.584
	GM	AD	1.579	1.703	1.582	1.613	1.628
		FA	2.614	2.651	2.557	3.004	3.167
		MD	1.624	1.748	1.627	1.613	1.602
		RD	1.694	1.809	1.698	1.659	1.627
NODDI CoV	WM	ICVF	2.585	2.854	2.584	2.676	1.68
		ODI	5.349	6.93	5.389	5.617	5.042
		ISOVF	15.54	15.96	15.54	16.74	14.41
	GM	ICVF	4.943	5.068	4.943	5.012	2.487
		ODI	1.776	1.77	1.78	1.982	1.792
		ISOVF	14.9	15.28	14.9	15.65	11.13
6-Direction DTI SCN MAE	WM	AD	0.3707	0.3186	0.3164	0.3494	0.3273
		FA	0.2163	0.1815	0.1643	0.1879	0.1544
		MD	0.2615	0.2691	0.2628	0.2632	0.2478
		RD	0.1703	0.2034	0.1646	0.1689	0.1593
	GM	AD	0.182	0.159	0.1654	0.1672	0.1613
		FA	0.2276	0.3128	0.2373	0.2104	0.1763
		MD	0.1399	0.1356	0.1381	0.138	0.136
		RD	0.127	0.1269	0.1306	0.13	0.1265
SCN Repeatability Error	WM	AD	0.1413	0.1479	0.1295	0.1384	0.134
		FA	0.1299	0.1231	0.1203	0.1247	0.1207
		MD	0.1386	0.1428	0.1387	0.1415	0.1378
		RD	0.1351	0.137	0.1309	0.1354	0.133
		ICVF	0.2528	0.1891	0.2524	0.2759	0.06437
		ODI	0.1364	0.05801	0.1356	0.1388	0.07944
		ISOVF	0.3568	0.3329	0.3568	0.3689	0.1298
	GM	AD	0.1547	0.1314	0.1737	0.1541	0.1494
		FA	0.1491	0.1062	0.2125	0.178	0.1636
		MD	0.1296	0.1275	0.1293	0.1272	0.1271
		RD	0.1253	0.1259	0.1239	0.1245	0.1229
		ICVF	0.5988	0.565	0.5987	0.6192	0.1017
		ODI	0.165	0.1688	0.1683	0.1652	0.1142
		ISOVF	0.5177	0.4929	0.5177	0.5255	0.1196

the lowest SCN repeatability error in WM for AD, FA, and RD estimation, while Patch2Self has the most repeatable SCN in WM for ODI estimation and GM for AD and FA estimation. Swin denoising has the lowest SCN repeatability error for MD, ICVF and ISOVF in WM as well as MD, RD, ICVF, ODI and ISOVF in GM. Once again, Swin performed remarkably better than all competing methods for ICVF and ISOVF, achieving CoV values that are one-sixth to one-third of those from no denoising or denoising with P2S, MPPCA or BM4D.

3.3 Clinical Validation

The Swin model achieves qualitatively superior denoising even in poor quality data ($\text{CNR} = 1.2375$), which was the lowest CNR in the AHA dataset (Fig. 2). Swin denoising conducted with only 6 directions approaches data quality achieved by acquiring all 55 directions, resulting in a 9-fold speedup of scan time. Applying Swin to all 55 directions removes much of the FA noise associated with the AVM and its surrounding hemorrhage. Fine-tuning leads to modest improvements in image quality for both the UNet and Swin models.

The Swin model, even with 6 directions, records DTI values which are consistent with those reported from other denoising algorithms with access to all 55 directions (Fig. S6). Swin is able to achieve lower FA than the other methods with only 6 directions, barring P2S which yields unrealistically low values for WM, showing Swin’s ability to reduce some of the noise which artifactualy inflates FA. In addition, apart from FA estimation in GM, Swin denoising generates similar values for both 6-direction and 55-direction acquisitions, indicating that tissue microstructural metrics remain consistent, even as the angular resolution is increased. The Swin model also consistently produces lower FA, MD, RD, and AD values than other denoising methods in the perilesional space across all three sessions in all subjects (Fig. S7). MPPCA, BM4D, and no denoising (RAW) tend to follow the same values.

3.4 Super-Resolution

Although our model was not trained for super-resolution, it can be used to resample a dMRI dataset to 1.25 mm resolution (Fig. 3). Qualitative comparison shows that Swin is able to capture more of the fine microstructure than BM4D and MPPCA in the posterior periventricular WM and avoids excessive blurring.

4 Discussion

To the best of the authors’ knowledge, this is the first supervised dMRI denoising method that can be applied, without modification, to denoise dMRI datasets with widely varying scanners, patient populations, and acquisition parameters. We have validated our approach on a held-out portion of the HCP dataset as well as three external OOD datasets consisting of children with neurodevelopmental disorders, adults with TBI, and both children and adolescents with intracranial

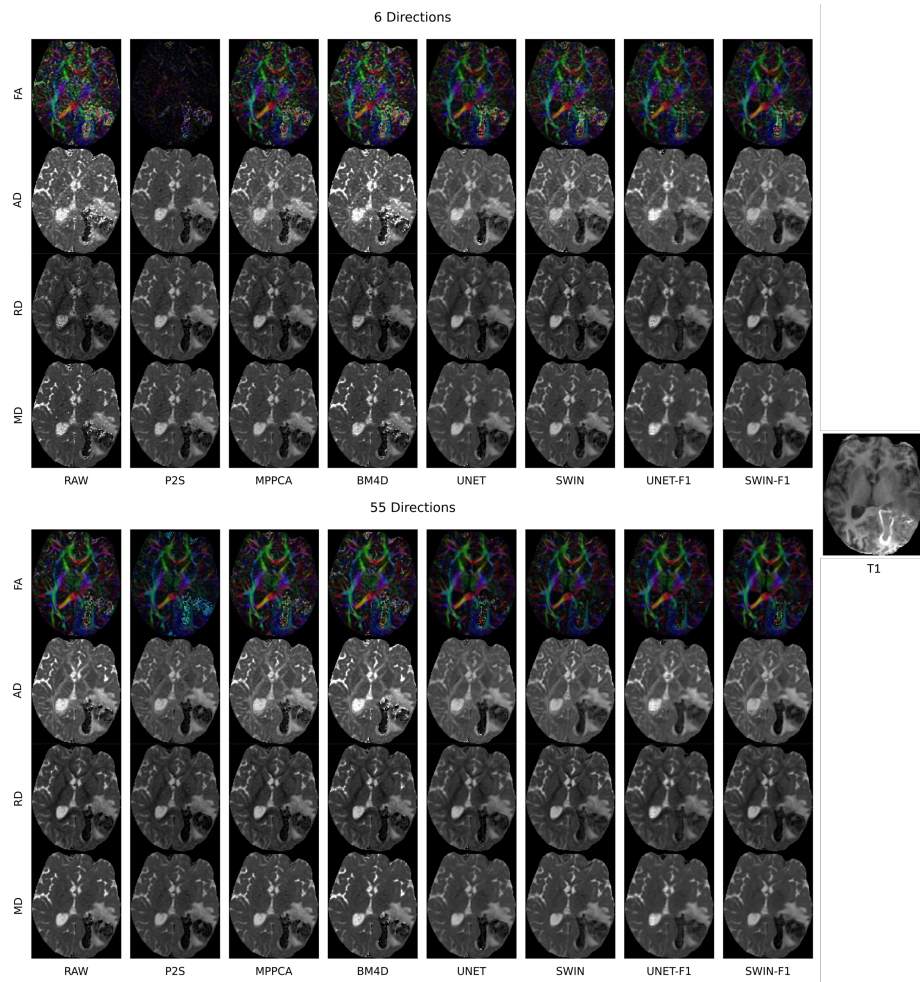


Fig. 2. Effect of denoising on a 6 direction subset as well as a full shell (55 directions) for a session with poor quality data: contrast-to-noise ratio (CNR) = 1.2375 measured by Eddy in FSL. DTI metrics derived from no denoising (RAW), Patch2Self (P2S), MPPCA, BM4D, UNet denoising without fine-tuning (UNET), and Swin denoising without fine-tuning (SWIN-F1), UNet denoising with fine-tuning (UNET-F1), and Swin denoising with fine-tuning (SWIN-F1) are displayed as well as the T1 anatomical image.

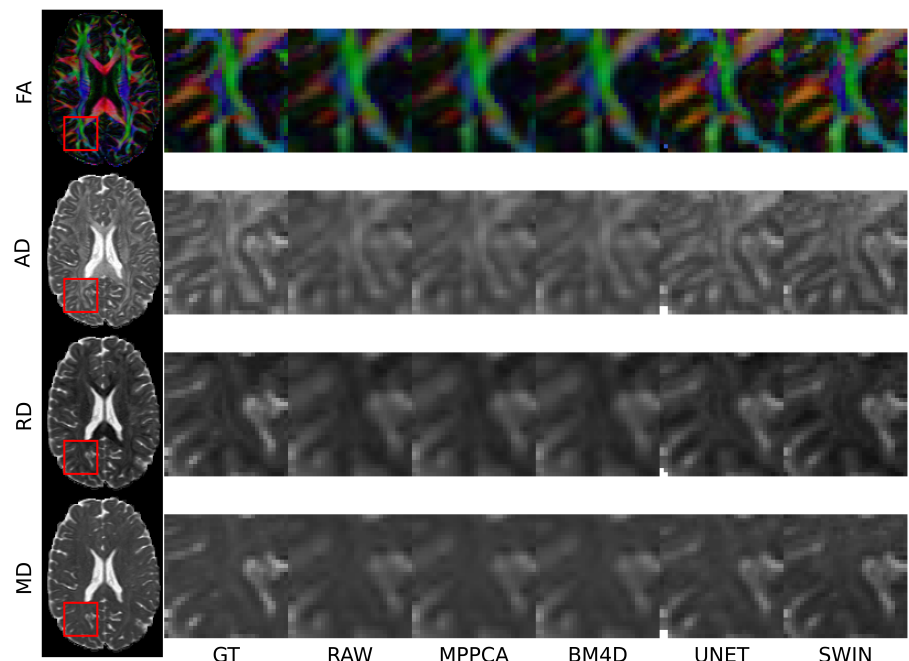


Fig. 3. Visual comparison between the ground truth (GT), no post-processing (RAW), MPPCA, BM4D, Unet, and Swin without fine-tuning (SWIN) for super-resolution in the posterior periventricular WM of an HCP subject. Data was k-space downsampled by a factor of two and then upsampled with 5th order spline interpolation back to 1.25 mm.

hemorrhage before and after resection of their vascular malformations. We have shown that our method can produce more accurate DTI metrics and spherical harmonic coefficients than other denoising methods with the minimum amount of data required for a unique fit. In addition, we have demonstrated the superior test-retest reliability of our denoising method for both DTI and NODDI metrics as well as SCNs derived from those metrics. Finally, we show that the Swin denoising has the potential to track brain microstructural changes with greater accuracy than other denoising models.

With Swin denoising, drastic scan time speedup is possible. Most dMRI protocols require at least $5 \text{ b}=0 \text{ s/mm}^2$ and $30 \text{ b}=1000 \text{ s/mm}^2$ acquisitions to obtain accurate DTI metrics, taking at least ten minutes [14]. With Swin denoising, a dMRI acquisition which can obtain accurate DTI metrics is easily achievable in under two minutes. In fact, such a minimal 6-direction acquisition would take 90 seconds with an HCP protocol, 100 seconds with the TBI or AHA protocol, and only 20 seconds with the SPIN protocol. This speedup can allow dMRI to be used clinically in vulnerable populations and would significantly reduce motion artifacts that degrade image quality.

The Swin model showed high repeatability in all cases, but especially for the NODDI metrics of tissue intracellular volume fraction and free water fraction, often achieving better than 50% lower CoV than the next best method. We believe that this could be due to the ability of the Swin model to have an approximately Gaussian output distribution. Unlike other denoising methods, the Swin model is able to remove the heavy tail noise inherent in dMRI data. Even BM4D, which is designed to correct for Rician noise, fails at this task. We believe that the Swin model and to a lesser extent the Unet succeed in this respect partly because, unlike other denoising models, they have access to the T1 anatomical image volume which aids in tissue segmentation, differentiating GM from WM from CSF. In addition, both models are trained to reduce mean-squared error, which heavily penalizes outliers and thus reduces the heavy tail.

There were cases where the Swin model was not the best. For instance, the Swin model performs worse than MPPCA in WM for 6th order spherical harmonic fitting, even in HCP data, possibly because the Swin model denoises one direction at a time, whereas MPPCA is able to collectively denoise all directions (Table S2). By processing each dMRI volume separately, we are able to consider the full brain volume and avoid artifact propagation across volumes but do not utilize the correlation across volumes, such as the transformer patch-based approach in [15]. Due to GPU memory constraints, a trade-off exists between utilizing spatial and angular correlations. Data compression techniques, such as quantized variational auto-encoders, should be explored to overcome this obstacle [8].

Our results were achieved with simple data augmentations, although using more extensive simulations, such as those in [21], could lead to greater generalizability. In addition, all inputs had to be resampled to 1.25 mm isotropic resolution, but with further data augmentation or resolution-independent architectures [5], it may be possible to perform denoising on native resolution if

super-resolution is not desired. Our results require a T1 anatomical scan to be acquired in conjunction with the dMRI data. While most datasets which have dMRI data also collect T1 scans, this might not always be the case and further work should be conducted to determine how important adding anatomical information, in the form of a T1 scan, is to denoising performance and whether T2 and other sequences can provide complementary information and further improve performance. Finally, our denoising method is designed to be performed after correction for patient movement, susceptibility-induced distortions, and eddy-current correction via the Eddy command as well as co-registration with a T1 scan. However, it may be fruitful to pursue 2D denoising which can clean raw data slice-by-slice to improve the performance of Eddy itself and yield better downstream results.

In addition, we trained a simple UNet which, while performing better than the other self-supervised methods, did not outperform the Swin model. This could be due to the ability of the Swin transformers to capture long-range dependencies better than a UNet, especially when provided with enough data [7]. It could also be because the same hyper-parameters were used for both the Swin and the UNet and those hyper-parameters were simply more optimal for the Swin model. Further investigation, with extensive hyper-parameter tuning on various datasets, would be necessary to determine the optimal architecture. In principle, we believe that most advanced neural network architectures, with sufficient complexity, would perform adequately.

We believe that some of the generalizability of our model may be attributed to grokking, a phenomenon that occurs when a neural network with good training loss but poor generalisation will, upon further training, transition to perfect generalisation [24]. We anecdotally observed grokking to occur after the sixth epoch of training and suspect this is due to using weight decay and AdamW adaptive stochastic gradient descent training on a sufficiently large dataset with data augmentation. A better understanding of what leads to grokking could be instrumental in designing generative AI models that generalize well at scale for healthcare.

Finally, fine-tuning on even one subject consistently led to improved denoising performance for DTI fitting, but the results were mixed in higher order spherical harmonic fitting. This could be because fine-tuning reduces model bias, but increases variance which can accumulate error over the 15 or 28 directions used to compute the 4th or 6th order spherical harmonics, respectively, compared to the six directions used in DTI estimation. In addition, we did not experience significant performance benefits by fine-tuning on more than one subject. Recent work has demonstrated that large language models can effectively learn from a single example and our model, while significantly smaller, might also exhibit similar behavior via successful domain adaptation with limited fine-tuning data. To the best of our knowledge, fine-tuning has never been reported before in the context of dMRI denoising and merits further investigation.

Acknowledgements. HCP data were provided by the Human Connectome Project, WU-Minn Consortium (Principal Investigators: David Van Essen and

Kamil Ugurbil; U54 MH091657) funded by the 16 NIH Institutes and Centers that support the NIH Blueprint for Neuroscience Research; and by the McDonnell Center for Systems Neuroscience at Washington University. TBI data were acquired as part of a research project funded by NIH R01NS060886 (Principal Investigator: Pratik Mukherjee). SPIN data were acquired as part of a research project funded by NIH R01 MH116950 (Principal Investigators: Pratik Mukherjee and Elysa J. Marco). AHA data were acquired with funding from the American Heart Association (AHA) Bugher Foundation (Principal Investigators: Heather Fullerton, Christine Fox, Helen Kim, and Pratik Mukherjee).

References

1. Andersson, J.L., Sotiroopoulos, S.N.: An integrated approach to correction for off-resonance effects and subject movement in diffusion mr imaging. *NeuroImage* **125**, 1063–1078 (1 2016). <https://doi.org/10.1016/J.NEUROIMAGE.2015.10.019>, <https://pubmed.ncbi.nlm.nih.gov/26481672/>
2. Billot, B., Magdamo, C., Arnold, S.E., Das, S., Iglesias, J.E.: Robust segmentation of brain mri in the wild with hierarchical cnns and no retraining. Lecture Notes in Computer Science (including subseries Lecture Notes in Artificial Intelligence and Lecture Notes in Bioinformatics) **13435 LNCS**, 538–548 (3 2022). <https://doi.org/10.48550/arxiv.2203.01969>, <https://arxiv.org/abs/2203.01969v3>
3. Cardoso, M.J., Li, W., Brown, R., Ma, N., Kerfoot, E., Wang, Y., Murrey, B., Myronenko, A., Zhao, C., Yang, D., Nath, V., He, Y., Xu, Z., Hatamizadeh, A., Myronenko, A., Zhu, W., Liu, Y., Zheng, M., Tang, Y., Yang, I., Zephyr, M., Hashemian, B., Alle, S., Darestani, M.Z., Budd, C., Modat, M., Vercauteren, T., Wang, G., Li, Y., Hu, Y., Fu, Y., Gorman, B., Johnson, H., Genereaux, B., Erdal, B.S., Gupta, V., Diaz-Pinto, A., Dourson, A., Maier-Hein, L., Jaeger, P.F., Baumgartner, M., Kalpathy-Cramer, J., Flores, M., Kirby, J., Cooper, L.A.D., Roth, H.R., Xu, D., Bericat, D., Floca, R., Zhou, S.K., Shuaib, H., Farahani, K., Maier-Hein, K.H., Aylward, S., Dogra, P., Ourselin, S., Feng, A.: Monai: An open-source framework for deep learning in healthcare. ArXiv (11 2022)
4. Cohen-Adad, J., Descoteaux, M., Wald, L.L.: Quality assessment of high angular resolution diffusion imaging data using bootstrap on q-ball reconstruction. *Journal of magnetic resonance imaging : JMRI* **33**, 1194 (5 2011). <https://doi.org/10.1002/JMRI.22535>, /pmc/articles/PMC3087444//pmc/articles/PMC3087444/?report=abstract<https://www.ncbi.nlm.nih.gov/pmc/articles/PMC3087444/>
5. Dehghani, M., Mustafa, B., Djolonga, J., Heek, J., Minderer, M., Caron, M., Steiner, A., Puigcerver, J., Geirhos, R., Alabdulmohsin, I., Oliver, A., Padlewski, P., Gritsenko, A., Lučić, M., Houlsby, N.: Patch n' pack: Navit, a vision transformer for any aspect ratio and resolution. ArXiv (7 2023), <http://arxiv.org/abs/2307.06304>
6. Derek K. Jones, P. (ed.): Diffusion MRI, vol. 1. Oxford University Press (9 2012). <https://doi.org/10.1093/med/9780195369779.001.0001>
7. Dosovitskiy, A., Beyer, L., Kolesnikov, A., Weissenborn, D., Zhai, X., Unterthiner, T., Dehghani, M., Minderer, M., Heigold, G., Gelly, S., Uszkoreit, J., Houlsby, N.: An image is worth 16x16 words: Transformers for image recognition at scale.

- ArXiv (10 2020). <https://doi.org/10.48550/arxiv.2010.11929>, <https://arxiv.org/abs/2010.11929v2>
8. Duan, Z., Lu, M., Ma, Z., Zhu, F.: Lossy image compression with quantized hierarchical vaes. pp. 198–207. IEEE (1 2023). <https://doi.org/10.1109/WACV56688.2023.00028>
 9. Essen, D.C.V., Smith, S.M., Barch, D.M., Behrens, T.E., Yacoub, E., Ugurbil, K.: The wu-minn human connectome project: An overview. NeuroImage **80**, 62 (10 2013). <https://doi.org/10.1016/J.NEUROIMAGE.2013.05.041>, /pmc/articles/PMC3724347//pmc/articles/PMC3724347/?report=abstract<https://www.ncbi.nlm.nih.gov/pmc/articles/PMC3724347/>
 10. Fadnavis, S., Batson, J., Garyfallidis, E.: Patch2self: Denoising diffusion mri with self-supervised learning. Advances in Neural Information Processing Systems **2020-Decem** (11 2020). <https://doi.org/10.48550/arxiv.2011.01355>, <https://arxiv.org/abs/2011.01355v1>
 11. Greve, D.N., Fischl, B.: Accurate and robust brain image alignment using boundary-based registration. NeuroImage **48**, 63 (10 2009). <https://doi.org/10.1016/J.NEUROIMAGE.2009.06.060>, /pmc/articles/PMC2733527//pmc/articles/PMC2733527/?report=abstract<https://www.ncbi.nlm.nih.gov/pmc/articles/PMC2733527/>
 12. Hatamizadeh, A., Nath, V., Tang, Y., Yang, D., Roth, H.R., Xu, D.: Swin unetr: Swin transformers for semantic segmentation of brain tumors in mri images. Lecture Notes in Computer Science (including subseries Lecture Notes in Artificial Intelligence and Lecture Notes in Bioinformatics) **12962 LNCS**, 272–284 (1 2022). <https://doi.org/10.48550/arxiv.2201.01266>, <https://arxiv.org/abs/2201.01266v1>
 13. Hoopes, A., Mora, J.S., Dalca, A.V., Fischl, B., Hoffmann, M.: Synth-strip: Skull-stripping for any brain image. NeuroImage **260** (3 2022). <https://doi.org/10.1016/j.neuroimage.2022.119474>, <http://arxiv.org/abs/2203.09974><http://dx.doi.org/10.1016/j.neuroimage.2022.119474>
 14. Jones, D.K.: The effect of gradient sampling schemes on measures derived from diffusion tensor mri: A monte carlo study. Magnetic Resonance in Medicine **51**, 807–815 (4 2004). <https://doi.org/10.1002/mrm.20033>
 15. Karimi, D., Gholipour, A.: Diffusion tensor estimation with transformer neural networks. Artificial Intelligence in Medicine **130** (1 2022). <https://doi.org/10.48550/arxiv.2201.05701>, <https://arxiv.org/abs/2201.05701v2>
 16. Li, Y.O., Yang, F.G., Nguyen, C.T., Cooper, S.R., LaHue, S.C., Venugopal, S., Mukherjee, P.: Independent component analysis of dti reveals multivariate microstructural correlations of white matter in the human brain. Human Brain Mapping **33**, 1431–1451 (6 2012). <https://doi.org/10.1002/hbm.21292>
 17. Liu, Z., Lin, Y., Cao, Y., Hu, H., Wei, Y., Zhang, Z., Lin, S., Guo, B.: Swin transformer: Hierarchical vision transformer using shifted windows. Proceedings of the IEEE International Conference on Computer Vision pp. 9992–10002 (3 2021). <https://doi.org/10.48550/arxiv.2103.14030>, <https://arxiv.org/abs/2103.14030v2>
 18. Loshchilov, I., Hutter, F.: Decoupled weight decay regularization. 7th International Conference on Learning Representations, ICLR 2019 (11 2017). <https://doi.org/10.48550/arxiv.1711.05101>, <https://arxiv.org/abs/1711.05101v3>

19. Lyu, Q., Shan, H., Wang, G.: Mri super-resolution with ensemble learning and complementary priors. *IEEE Transactions on Computational Imaging* **6**, 615–624 (7 2019). <https://doi.org/10.1109/TCI.2020.2964201>, <http://arxiv.org/abs/1907.03063><http://dx.doi.org/10.1109/TCI.2020.2964201>
20. Maggioni, M., Katkovnik, V., Egiazarian, K., Foi, A.: Nonlocal transform-domain filter for volumetric data denoising and reconstruction. *IEEE Transactions on Image Processing* **22**, 119–133 (2013). <https://doi.org/10.1109/TIP.2012.2210725>
21. Muckley, M.J., Ades-Aron, B., Papaioannou, A., Lemberskiy, G., Solomon, E., Lui, Y.W., Sodickson, D.K., Fieremans, E., Novikov, D.S., Knoll, F.: Training a neural network for gibbs and noise removal in diffusion mri. *Magnetic resonance in medicine* **85**, 413 (1 2021). <https://doi.org/10.1002/MRM.28395>, /pmc/articles/PMC7722184//pmc/articles/PMC7722184/?report=abstract<https://www.ncbi.nlm.nih.gov/pmc/articles/PMC7722184/>
22. Mukherjee, P., Chung, S., Berman, J., Hess, C., Henry, R.: Diffusion tensor mr imaging and fiber tractography: Technical considerations. *American Journal of Neuroradiology* **29**, 843–852 (5 2008). <https://doi.org/10.3174/ajnr.A1052>
23. Paszke, A., Gross, S., Massa, F., Lerer, A., Bradbury, J., Chanan, G., Killeen, T., Lin, Z., Gimelshein, N., Antiga, L., Desmaison, A., Köpf, A., Yang, E., DeVito, Z., Raison, M., Tejani, A., Chilamkurthy, S., Steiner, B., Fang, L., Bai, J., Chintala, S.: Pytorch: An imperative style, high-performance deep learning library. *ArXiv* (12 2019)
24. Power, A., Burda, Y., Edwards, H., Babuschkin, I., Misra, V.: Grokking: Generalization beyond overfitting on small algorithmic datasets. *ArXiv* (1 2022)
25. Skare, S., Hedehus, M., Moseley, M.E., Li, T.Q.: Condition number as a measure of noise performance of diffusion tensor data acquisition schemes with mri. *Journal of Magnetic Resonance* **147**, 340–352 (12 2000). <https://doi.org/10.1006/jmre.2000.2209>
26. Smith, S.M., Jenkinson, M., Johansen-Berg, H., Rueckert, D., Nichols, T.E., Mackay, C.E., Watkins, K.E., Ciccarelli, O., Cader, M.Z., Matthews, P.M., Behrens, T.E.: Tract-based spatial statistics: Voxelwise analysis of multi-subject diffusion data. *NeuroImage* **31**, 1487–1505 (7 2006). <https://doi.org/10.1016/j.neuroimage.2006.02.024>
27. Tian, Q., Bilgic, B., Fan, Q., Liao, C., Ngamsombat, C., Hu, Y., Witzel, T., Setsompop, K., Polimeni, J.R., Huang, S.Y.: Deepdti: High-fidelity six-direction diffusion tensor imaging using deep learning. *NeuroImage* **219**, 117017 (10 2020). <https://doi.org/10.1016/J.NEUROIMAGE.2020.117017>, /pmc/articles/PMC7646449//pmc/articles/PMC7646449/?report=abstract<https://www.ncbi.nlm.nih.gov/pmc/articles/PMC7646449/>
28. Tian, Q., Li, Z., Fan, Q., Polimeni, J.R., Bilgic, B., Salat, D.H., Huang, S.Y.: Sndti: Self-supervised deep learning-based denoising for diffusion tensor mri. *NeuroImage* **253** (6 2022). <https://doi.org/10.1016/J.NEUROIMAGE.2022.119033>, <https://pubmed.ncbi.nlm.nih.gov/35240299/>
29. Veraart, J., Novikov, D.S., Christiaens, D., Ades-aron, B., Sijbers, J., Fieremans, E.: Denoising of diffusion mri using random matrix theory. *NeuroImage* **142**, 394 (11 2016). <https://doi.org/10.1016/J.NEUROIMAGE.2016.08.016>, /pmc/articles/PMC5159209//pmc/articles/PMC5159209/?report=abstract<https://www.ncbi.nlm.nih.gov/pmc/articles/PMC5159209/>
30. Wahl, M., Li, Y.O., Ng, J., LaHue, S.C., Cooper, S.R., Sherr, E.H., Mukherjee, P.: Microstructural correlations of white matter tracts in the human brain. *NeuroImage* **51**, 531–541 (6 2010). <https://doi.org/10.1016/J.NEUROIMAGE.2010.02.072>, <https://pubmed.ncbi.nlm.nih.gov/20206699/>

31. Zhang, H., Schneider, T., Wheeler-Kingshott, C.A., Alexander, D.C.: Noddi: Practical *in vivo* neurite orientation dispersion and density imaging of the human brain. *NeuroImage* **61**, 1000–1016 (7 2012). <https://doi.org/10.1016/j.neuroimage.2012.03.072>

Generative AI for Rapid Diffusion MRI with Improved Image Quality, Reliability and Generalizability Supplementary

Amir Sadikov¹², Xinlei Pan³, Hannah Choi¹, Lanya T. Cai¹, and Pratik Mukherjee¹²

¹ Radiology and Biomedical Imaging, University of California, San Francisco

² Graduate Group in Bioengineering, University of California, San Francisco

³ University of California, Berkeley

amir.sadikov@ucsf.edu

1 Introduction

For a list of all abbreviations used in the manuscript and their definitions, see Table S1.

Table S1: Table of Abbreviations

Abbreviation	Definition
dMRI	Diffusion MRI
DTI	Diffusion Tensor Imaging
NODDI	Neurite Orientation Dispersion and Density Imaging
SCN	Structural Covariance Network
HCP	Human Connectome Project
AHA	American Heart Association
TBSS	Tract-Based Spatial Statistics
JHU	Johns Hopkins University
MAE	Mean Absolute Error
JSD	Jensen–Shannon Distance
CoV	Coefficient of Variation
SNR	Signal-to-Noise Ratio
CNR	Contrast-to-Noise Ratio
OOD	Out-Of-Domain
WM	White Matter
GM	Gray Matter
GT	Ground Truth
RAW	No Denoising Applied
BM4D	Block-Matching and 4D filtering
MPPCA	Marchenko-Pastur Principal Component Analysis
P2S	Patch2Self
UNET-F1	UNET with fine-tuning on one subject
Swin UNETR/SWIN	Swin UNET TRansformers

SWIN-F1	SWIN with fine-tuning on one subject
V1	Principal Eigenvector
FA	Fractional Anisotropy
AD	Axial Diffusivity
RD	Radial Diffusivity
MD	Mean Diffusivity
ICVF	Intracellular Volume Fraction
ODI	fiber Orientation Dispersion Index
ISOVF	Free Water Fraction
MCP	Middle Cerebellar Peduncle
PCT	Pontine Crossing Tract
GCC	Genu of Corpus Callosum
BCC	Body of Corpus callosum
SCC	Splenium of corpus callosum
FX	Fornix
CST	Corticospinal Tract
ML	Medial Lemniscus
ICP	Inferior Cerebellar Peduncle
SCP	Superior Cerebellar Peduncle
CP	Cerebral Peduncle
ALIC	Anterior Limb of Internal Capsule
PLIC	Posterior Limb of Internal Capsule
RLIC	Retrolenticular Limb of Internal Capsule
ACR	Anterior Corona Radiata
SCR	Superior Corona Radiata
PCR	Posterior Corona Radiata
PTR	Posterior Thalamic Radiation
SS	Sagittal Stratum
EC	External Capsule
CGC	Cingulum (Cingulate Gyrus)
CGH	Cingulum (Parahippocampal)
FXST	fornix and Stria Terminalis
SLF	Superior Longitudinal Fasciculus
SFO	Superior Fronto-Occipital Fasciculus
UNC	Uncinate Fasciculus
TPT	Tapetum

2 Methods

A mask for the perilesional space was found by taking the largest connected component of the region that Freesurfer *recon-all* segments as "*unknown*" inside the brain mask. We dilate this mask two-fold and only take the dilated portion to be perilesional.

3 Results

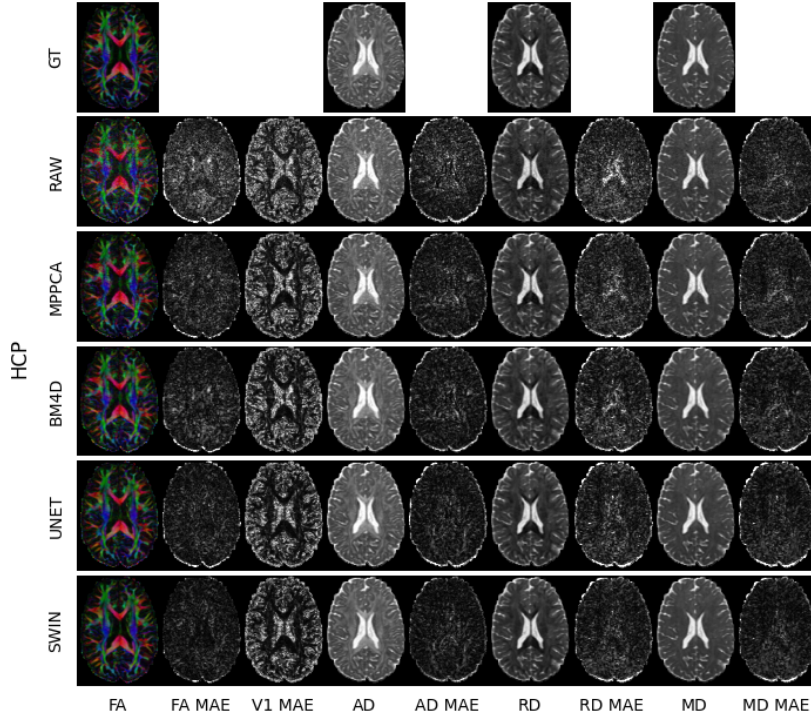


Fig. S1. Visual comparison between the ground truth (GT), no denoising (RAW), BM4D, MPPCA, Unet, and Swin without finetuning (SWIN) for denoising on validation data from the HCP dataset

For 4th and 6th order spherical harmonic fitting, the Swin model achieves the lowest JSD in GM across all datasets (Table S2). In particular, the Swin model outperforms all other denoising methods in the external datasets (AHA, TBI, SPIN) with the exception of 6th order estimation of B1000 WM spherical harmonics in SPIN and B2000 WM spherical harmonics in AHA, where no denoising has the lowest JSD. For the HCP dataset, the MPPCA had a lower JSD than the Swin model for 6th order spherical harmonic estimation in higher shells. The Unet model achieves lower JSD than the Swin model in several metrics in the HCP dataset, but performs worse in the external datasets.

The Swin model is able to achieve lower byte-lengths of dMRI data compressed with zlib using both high and low compression levels (Table S3).

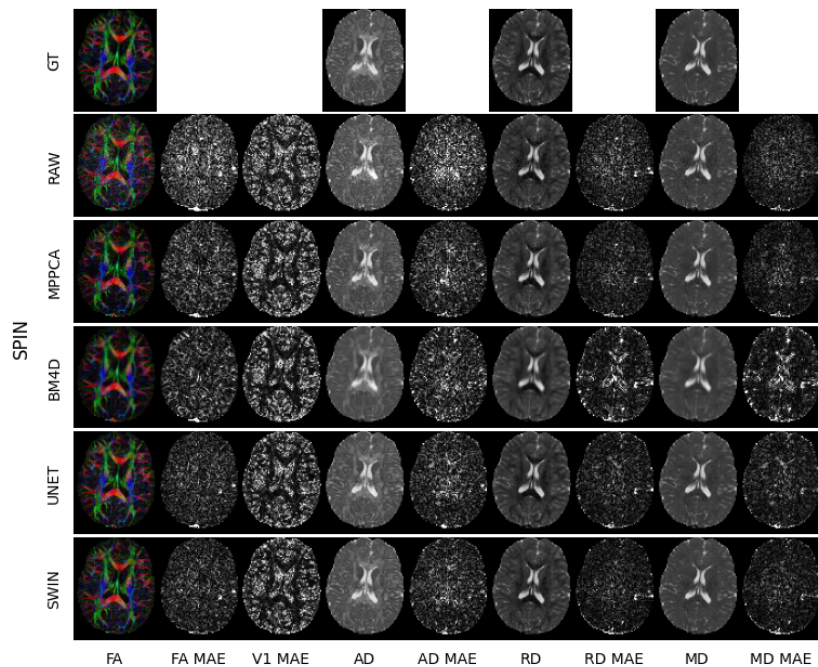


Fig. S2. Visual comparison between the ground truth (GT), no denoising (RAW), BM4D, MPPCA, Unet, and Swin without finetuning (SWIN) for denoising on validation data from the SPIN dataset

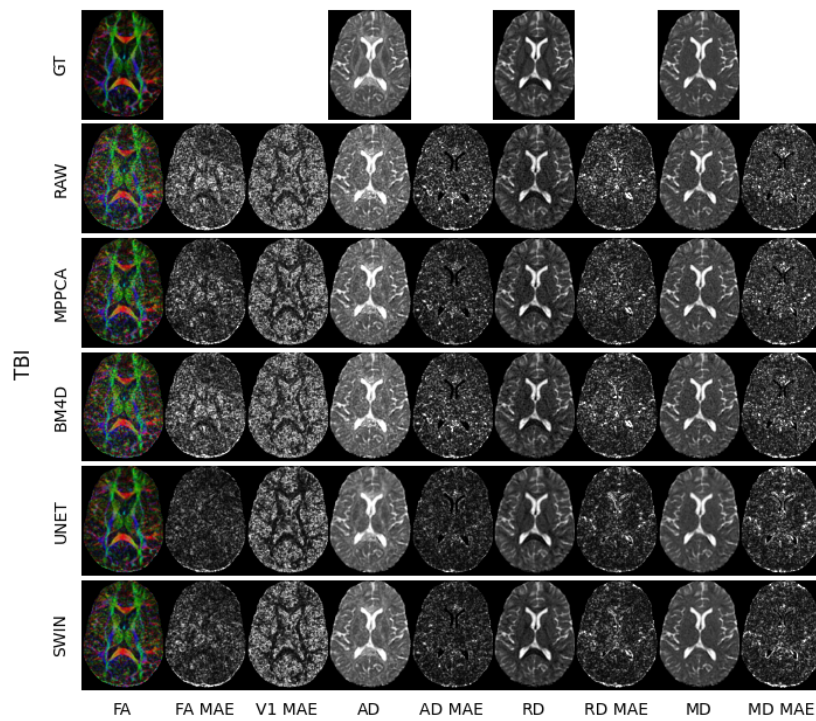


Fig. S3. Visual comparison between the ground truth (GT), no denoising (RAW), BM4D, MPPCA, UNET, and Swin without finetuning (SWIN) for denoising on validation data from the TBI dataset

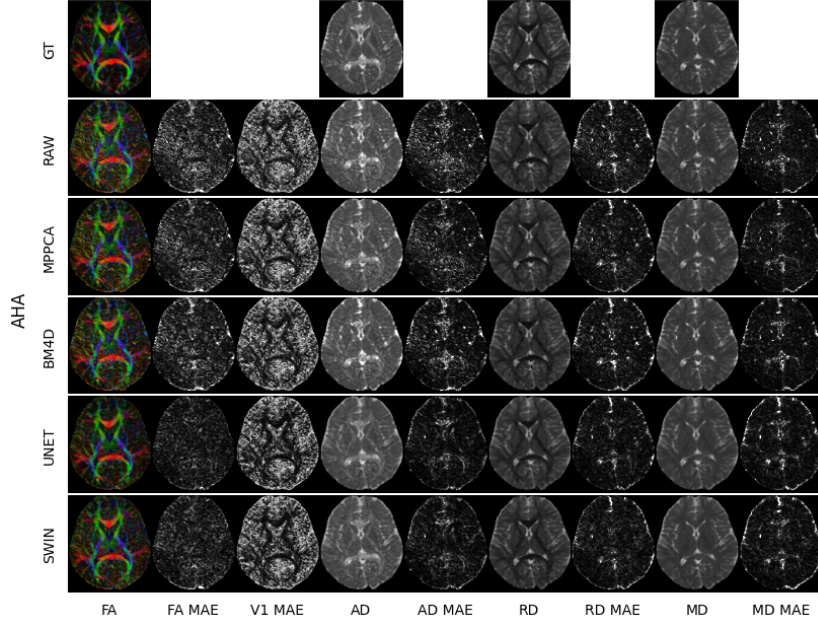


Fig. S4. Visual comparison between the ground truth (GT), no denoising (RAW), BM4D, MPPCA, UNET, and Swin without finetuning (SWIN) for denoising on validation data from the AHA dataset

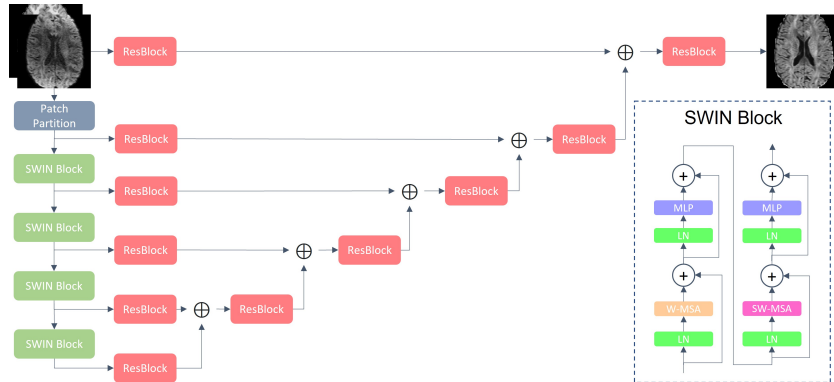


Fig. S5. A general overview of the Swin-UNETR architecture. The input is a concatenated 3D T1 and dMRI scan, which is encoded by a Swin transformer at multiple resolutions and fed into a residual convolutional neural net (CNN) decoder to reconstruct the ground truth dMRI scan.

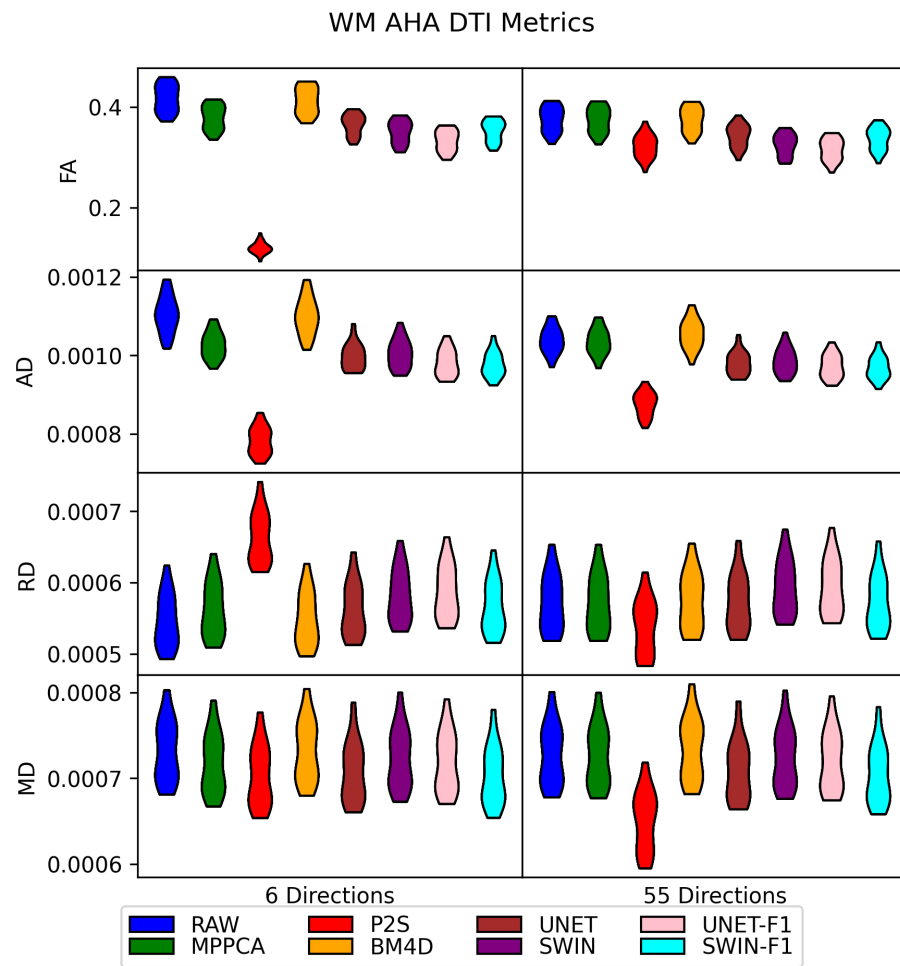


Fig. S6. DTI metrics in WM and GM from no denoising (RAW), MPPCA, BM4D, and Swin denoising for 6 direction and 55 direction subsets from the AHA $b=2000$ s/mm^2 shell.

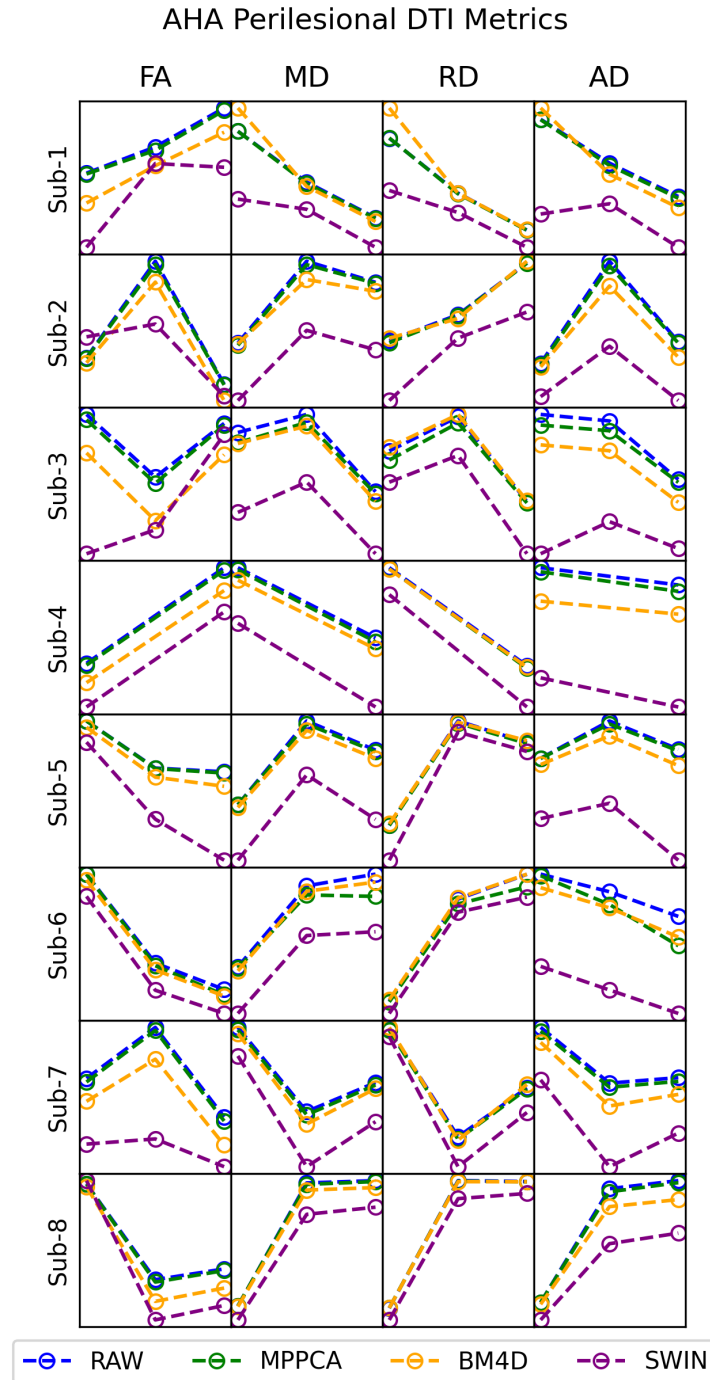


Fig. S7. Average DTI metrics (AD, FA, MD, RD) from denoising dMRI data in the perilesional space of AHA subjects across three sessions: first session data is taken one day prior to AVM resection, second session data is taken 6 months after AVM resection, and third session is taken one year after AVM resection. Subject 4 has data from only sessions one and three.

Table S2. JSD between ground truth and estimation using 15-direction (4th order) and 28-direction (6th order) HCP, SPIN, TBI, and AHA data in white matter (WM) and gray matter (GM) via no denoising (RAW), P2S, BM4D, MPPCA, UNET, and SWIN (with and without no finetuning). Best results are **bolded**.

Site	Order	Shell	Tissue	RAW	P2S	MPPCA	BM4D	UNET	SWIN	UNET-F1	SWIN-F1
HCP	4th	B1000	WM	0.0279	0.0385	0.0264	0.0257	0.0246	0.0251		
			GM	0.0232	0.023	0.0208	0.0208	0.019	0.0184		
		B2000	WM	0.0423	0.0627	0.0396	0.0382	0.038	0.0383		
	6th	B2000	GM	0.0365	0.0396	0.0317	0.0309	0.0292	0.0286		
			WM	0.0522	0.0742	0.0477	0.0459	0.0461	0.0458		
		B3000	GM	0.0486	0.047	0.0401	0.039	0.0371	0.0364		
	6th	B1000	WM	0.0206	0.0268	0.0203	0.0209	0.0199	0.0205		
			GM	0.0179	0.019	0.0173	0.0178	0.0158	0.0157		
		B2000	WM	0.0309	0.0432	0.03	0.0306	0.0307	0.0313		
TBI	4th	B1000	GM	0.0284	0.0307	0.0266	0.027	0.0249	0.0252		
			WM	0.0378	0.0526	0.036	0.0365	0.0375	0.0376		
	6th	B1000	GM	0.0377	0.0383	0.0342	0.0345	0.0322	0.0327		
			WM	0.0395	0.0566	0.0396	0.0408	0.0356	0.0354	0.0369	0.0363
SPIN	4th	B1000	GM	0.0361	0.0357	0.0361	0.0374	0.0311	0.0319	0.0313	0.0305
			WM	0.0269	0.0408	0.0278	0.0284	0.0274	0.0262	0.0288	0.0287
		B2500	GM	0.026	0.03	0.0269	0.0277	0.0247	0.0244	0.0248	0.0247
			WM	0.0481	0.0909	0.0472	0.0526	0.0461	0.0449	0.0468	0.0436
	6th	B1000	GM	0.0392	0.073	0.0362	0.0377	0.0336	0.0334	0.0337	0.0328
			WM	0.0179	0.0303	0.019	0.0282	0.0189	0.0187	0.0204	0.0183
		B2500	GM	0.0154	0.0243	0.0164	0.0208	0.0151	0.0149	0.0152	0.0147
			WM	0.0344	0.056	0.0347	0.0442	0.0356	0.0343	0.0368	0.0338
AHA	4th	B2000	GM	0.0429	0.0597	0.0424	0.0482	0.0469	0.0457	0.0501	0.0474
			WM	0.0301	0.0537	0.0309	0.0313	0.0328	0.0305	0.0368	0.0346
	6th	B2000	GM	0.0299	0.0523	0.0307	0.031	0.0301	0.0295	0.0307	0.0307

Table S3. The sum of all dMRI data byte-lengths in Gb for the HCP test-retest diffusion dataset undergoing no denoising (RAW), Patch2Self (P2S), MPPCA, BM4D, and Swin denoising compressed with lzib, using the DEFLATE algorithm, with compression levels of 1 (lowest) and 9 (highest). Best results are **bolded**.

Compression Level	RAW	P2S	MPPCA	BM4D	SWIN
1	64.3381	64.0960	64.3384	64.1420	64.0651
9	62.5757	62.2917	62.5755	62.3479	62.2508

Table S4: Coefficient of variation (%) for FA estimation via no denoising (RAW), P2S, BM4D, MPPCA, and SWIN for gray matter cortical regions in HCP test-retest data. Best results are **bolded**.

Cortical Regions	GT	RAW	P2S	MPPCA	BM4D	SWIN
lh-bankssts	2.172	4.164	5.232	5.394	4.023	3.46
lh-caudalanteriorcingulate	2.802	5.007	6.701	6.667	4.382	4.095
lh-caudalmiddlefrontal	3.514	4.353	5.843	5.293	3.614	3.521
lh-cuneus	2.675	4.051	5.03	6.597	4.95	3.906
lh-entorhinal	3.157	4.179	7.537	8.49	5.477	5.085
lh-fusiform	1.889	3.047	4.621	5.696	3.455	3.032
lh-inferiorparietal	1.914	3.867	4.831	4.777	3.73	3.492
lh-inferiortemporal	1.697	4.773	6.379	8.81	6.449	6.011
lh-isthmuscingulate	2.853	3.817	5.559	4.998	3.717	3.434
lh-lateraloccipital	1.654	5.627	6.669	6.512	5.329	5.046
lh-lateralorbitofrontal	2.88	4.293	6.806	8.264	6.126	5.416
lh-lingual	1.838	4.395	5.43	5.654	4.015	3.81
lh-medialorbitofrontal	4.268	5.172	7.835	11.19	8.096	7.244
lh-middletemporal	1.785	3.351	5.036	5.292	3.855	3.137
lh-parahippocampal	2.998	3.247	5.219	4.891	3.174	3.282
lh-paracentral	2.788	4.242	5.375	4.333	3.319	3.004
lh-parsopercularis	1.966	4.545	5.79	5.412	3.873	3.503
lh-parsorbitalis	2.785	5.035	8.17	8.675	6.46	5.678
lh-parstriangularis	2.673	5.211	6.794	6.327	5.119	4.683
lh-pericalcarine	3.738	4.472	5.2	5.83	4.284	3.715
lh-postcentral	2.074	4.458	5.112	3.899	3.582	3.251
lh-posteriorcingulate	1.928	4.368	5.797	5.541	3.221	3.283
lh-precentral	2.438	4.124	5.052	3.538	2.947	2.823
lh-precuneus	1.29	3.66	4.392	4.286	3.076	2.436
lh-rostralanteriorcingulate	2.155	4.06	5.689	6.188	3.87	3.652
lh-rostralmiddlefrontal	2.878	5.38	6.803	6.284	5.29	4.746
lh-superiorfrontal	2.057	4.547	5.484	4.945	3.38	3.09
lh-superiorparietal	3.014	3.949	4.874	4.674	3.571	3.418
lh-superiortemporal	1.687	3.181	4.776	4.482	3.31	3.297
lh-supramarginal	1.6	3.783	4.945	3.909	3.41	3.074
lh-frontalpole	3.495	10.45	11.46	14.11	11.6	10.4
lh-temporalpole	3.84	5.668	7.955	9.413	6.697	6.286
lh-transversetemporal	2.492	3.941	4.808	6.848	4.606	4.2
lh-insula	2.699	3.06	4.275	3.823	3.256	3.333
rh-bankssts	1.679	3.502	4.737	5.036	3.836	3.36
rh-caudalanteriorcingulate	3.754	3.832	5.278	5.682	3.953	3.577
rh-caudalmiddlefrontal	2.839	4.993	6.568	4.9	3.655	3.624
rh-cuneus	3.285	3.761	4.869	4.768	3.511	3.783
rh-entorhinal	2.655	5.17	6.853	10.34	7.656	7.398
rh-fusiform	1.556	3.004	4.721	7.11	4.116	3.803

rh-inferiorparietal	1.577	4.095	5.737	3.827	3.447	3.249
rh-inferiortemporal	2.19	4.019	5.732	9.235	5.782	5.198
rh-isthmuscingulate	3.297	3.538	5.597	5.21	3.605	3.295
rh-lateraloccipital	1.483	5.326	6.906	6.12	5.093	4.467
rh-lateralorbitofrontal	3.025	3.649	6.27	7.66	4.896	4.461
rh-lingual	2.591	3.648	5.079	5.146	3.422	3.49
rh-medialorbitofrontal	3.865	5.22	6.977	9.224	7.26	6.678
rh-middletemporal	2.347	4.295	5.019	6.99	4.56	4.009
rh-parahippocampal	2.034	3.577	5.011	6.949	3.945	4.267
rh-paracentral	5.078	3.526	4.215	5.596	3.67	4.639
rh-parsopercularis	2.042	3.875	5.308	4.527	2.995	2.881
rh-parsorbitalis	3.394	6.082	7.149	10.66	7.513	6.845
rh-parstriangularis	3.418	4.89	5.84	6.77	4.735	4.57
rh-pericalcarine	2.601	3.61	4.901	4.31	3.816	3.304
rh-postcentral	2.064	4.4	5.181	3.945	3.16	2.99
rh-posteriorcingulate	3.623	3.635	5.461	5.343	3.468	3.577
rh-precentral	2.099	3.926	4.932	3.335	2.391	2.568
rh-precuneus	3.332	3.356	4.715	4.021	2.689	2.654
rh-rostralanteriorcingulate	2.957	3.886	5.155	5.762	3.591	3.376
rh-rostralmiddlefrontal	3.14	5.465	6.431	6.758	4.821	4.266
rh-superiorfrontal	2.647	4.873	5.732	5.123	3.198	3.076
rh-superiorparietal	1.542	4.339	5.296	4.48	3.519	3.242
rh-superiortemporal	1.798	2.978	4.381	5.179	3.259	3.086
rh-supramarginal	1.828	3.413	4.906	3.71	2.767	2.47
rh-frontalpole	3.748	9.115	11.02	14.46	11.46	10.14
rh-temporalpole	3.801	6.287	7.234	12.14	8.362	7.879
rh-transversetemporal	3.085	3.805	4.704	7.426	4.481	4.681
rh-insula	1.654	2.262	3.813	3.394	2.082	1.879

Table S5: Coefficient of variation (%) for MD estimation via no denoising (RAW), P2S, BM4D, MPPCA, and SWIN for gray matter cortical regions in HCP test-retest data. Best results are **bolded**.

Cortical Regions	GT	RAW	P2S	MPPCA	BM4D	SWIN
lh-bankssts	1.072	2.048	2.02	2.054	2.022	1.957
lh-caudalanteriorcingulate	1.677	2.419	2.409	2.427	2.361	2.331
lh-caudalmiddlefrontal	1.333	2.277	2.308	2.274	2.243	2.122
lh-cuneus	1.498	2.096	2.08	2.092	2.081	2.108
lh-entorhinal	2.644	4.279	4.369	4.381	4.351	4.296
lh-fusiform	0.9479	1.732	1.759	1.755	1.776	1.67
lh-inferiorparietal	1.415	2.292	2.27	2.294	2.302	2.195
lh-inferiortemporal	1.121	2.799	2.835	2.828	2.821	2.639
lh-isthmuscingulate	1.486	2.491	2.483	2.458	2.477	2.454
lh-lateraloccipital	1.475	2.522	2.598	2.548	2.565	2.507

lh-lateralorbitofrontal	1.771	3.255	3.404	3.427	3.426	3.306
lh-lingual	1.512	1.895	1.888	1.876	1.919	1.828
lh-medialorbitofrontal	2.745	4.605	4.695	4.801	4.774	4.31
lh-middletemporal	1.312	2.328	2.357	2.341	2.326	2.292
lh-parahippocampal	1.178	2.675	2.625	2.657	2.68	2.684
lh-paracentral	1.781	2.297	2.294	2.285	2.244	2.128
lh-parsopercularis	1.403	1.862	1.882	1.852	1.84	1.788
lh-parsorbitalis	1.666	3.204	3.168	3.224	3.25	2.982
lh-parstriangularis	1.702	1.948	2.011	1.954	1.962	1.941
lh-pericalcarine	1.46	2.141	2.148	2.133	2.099	2.07
lh-postcentral	1.534	2.141	2.131	2.139	2.092	2.055
lh-posteriorcingulate	1.389	2.045	2.094	2.065	2.03	1.922
lh-precentral	1.402	2.023	2.056	2.023	2.015	1.923
lh-precuneus	1.16	1.828	1.789	1.815	1.788	1.781
lh-rostralanteriorcingulate	1.736	2.739	2.725	2.751	2.734	2.656
lh-rostralmiddlefrontal	1.479	2.132	2.098	2.144	2.122	2.062
lh-superiorfrontal	1.293	1.713	1.741	1.717	1.678	1.685
lh-superiorparietal	1.531	2.322	2.3	2.309	2.297	2.219
lh-superiortemporal	1.084	2.021	2.043	2.008	2.017	1.972
lh-supramarginal	1.197	1.878	1.87	1.872	1.86	1.836
lh-frontalpole	4.041	7.534	7.535	7.627	7.503	7.034
lh-temporalpole	3.18	3.808	3.881	3.869	3.933	3.849
lh-transversetemporal	1.608	2.614	2.578	2.585	2.513	2.489
lh-insula	1.035	1.917	1.913	1.921	1.912	1.909
rh-bankssts	1.127	2.185	2.184	2.18	2.177	2.13
rh-caudalanteriorcingulate	1.12	1.419	1.455	1.412	1.411	1.403
rh-caudalmiddlefrontal	1.558	2.149	2.177	2.135	2.077	1.943
rh-cuneus	1.478	2.446	2.443	2.428	2.404	2.418
rh-entorhinal	1.971	3.506	3.58	3.57	3.544	3.465
rh-fusiform	1.474	2.265	2.261	2.231	2.281	2.13
rh-inferiorparietal	1.337	2.23	2.207	2.208	2.178	2.108
rh-inferiortemporal	1.989	2.687	2.803	2.757	2.78	2.569
rh-isthmuscingulate	1.073	2.137	2.092	2.135	2.13	2.086
rh-lateraloccipital	1.818	2.524	2.461	2.498	2.493	2.365
rh-lateralorbitofrontal	2.297	3.217	3.227	3.281	3.332	3.25
rh-lingual	1.389	2.401	2.363	2.399	2.384	2.328
rh-medialorbitofrontal	2.521	4.382	4.53	4.591	4.662	4.196
rh-middletemporal	1.639	2.55	2.568	2.551	2.552	2.493
rh-parahippocampal	0.9239	2.308	2.325	2.302	2.294	2.169
rh-paracentral	2.01	2.207	2.178	2.191	2.212	2.132
rh-parsopercularis	1.481	1.801	1.755	1.796	1.781	1.873
rh-parsorbitalis	2.493	3.234	3.101	3.217	3.269	3.108
rh-parstriangularis	2.04	2.874	2.835	2.872	2.841	2.893
rh-pericalcarine	1.463	2.114	2.127	2.123	2.084	2.127
rh-postcentral	1.334	1.617	1.61	1.616	1.572	1.477

rh-posteriorcingulate	1.159	1.675	1.69	1.676	1.675	1.578
rh-precentral	1.38	1.847	1.853	1.842	1.79	1.666
rh-precuneus	1.156	1.737	1.71	1.729	1.715	1.701
rh-rostralanteriorcingulate	1.4	1.961	1.951	1.961	1.942	1.875
rh-rostralmiddlefrontal	1.934	2.609	2.554	2.605	2.574	2.594
rh-superiorfrontal	1.334	1.844	1.88	1.829	1.8	1.656
rh-superiorparietal	1.422	2.38	2.373	2.378	2.336	2.256
rh-superiortemporal	1.363	1.717	1.741	1.712	1.679	1.732
rh-supramarginal	1.203	1.921	1.899	1.913	1.87	1.836
rh-frontalpole	3.252	6.283	6.368	6.38	6.38	5.716
rh-temporalpole	2.565	2.85	3.062	3.146	3.18	3.192
rh-transversetemporal	1.749	2.591	2.564	2.573	2.503	2.525
rh-insula	1.135	1.689	1.686	1.674	1.692	1.665

Table S6: Coefficient of variation (%) for RD estimation via no denoising (RAW), P2S, BM4D, MPPCA, and SWIN for gray matter cortical regions in HCP test-retest data. Best results are **bolded**.

Cortical Regions	GT	RAW	P2S	MPPCA	BM4D	SWIN
lh-bankssts	1.098	2.347	2.138	2.268	2.247	2.023
lh-caudalanteriorcingulate	1.71	2.912	2.624	2.689	2.603	2.51
lh-caudalmiddlefrontal	1.422	2.41	2.322	2.343	2.323	2.229
lh-cuneus	1.624	2.36	2.105	2.356	2.334	2.335
lh-entorhinal	2.76	4.89	4.634	4.642	4.687	4.591
lh-fusiform	0.9626	1.898	1.831	1.964	1.931	1.782
lh-inferiorparietal	1.464	2.375	2.314	2.418	2.393	2.331
lh-inferiortemporal	1.109	3.07	2.95	3.069	3.079	2.878
lh-isthmuscingulate	1.699	2.828	2.572	2.878	2.845	2.721
lh-lateraloccipital	1.507	2.808	2.684	2.679	2.703	2.688
lh-lateralorbitofrontal	1.774	3.952	3.587	3.809	3.832	3.717
lh-lingual	1.577	2.159	1.983	2.064	2.048	1.946
lh-medialorbitofrontal	2.774	5.154	4.945	4.889	5.041	4.539
lh-middletemporal	1.361	2.46	2.43	2.439	2.452	2.425
lh-parahippocampal	1.411	2.931	2.744	2.912	2.888	2.89
lh-paracentral	1.907	2.381	2.288	2.362	2.3	2.197
lh-parsopercularis	1.473	2.019	1.891	1.955	1.921	1.906
lh-parsorbitalis	1.693	3.678	3.341	3.7	3.678	3.286
lh-parstriangularis	1.775	2.371	2.014	2.334	2.326	2.237
lh-pericalcarine	1.612	2.331	2.186	2.286	2.184	2.163
lh-postcentral	1.592	2.229	2.138	2.172	2.15	2.1
lh-posteriorcingulate	1.469	2.47	2.241	2.201	2.163	2.066
lh-precentral	1.528	2.122	2.066	2.124	2.117	2.039
lh-precuneus	1.229	1.864	1.799	1.865	1.827	1.855
lh-rostralanteriorcingulate	1.735	3.135	2.814	3.037	2.966	2.835

lh-rostralmiddlefrontal	1.46	2.415	2.21	2.319	2.333	2.218
lh-superiorfrontal	1.241	1.931	1.773	1.842	1.812	1.789
lh-superiorparietal	1.623	2.34	2.3	2.409	2.358	2.347
lh-superiortemporal	1.128	2.063	2.082	2.086	2.085	2.042
lh-supramarginal	1.254	1.951	1.894	1.959	1.934	1.908
lh-frontalpole	3.976	8.321	7.799	7.921	7.903	7.384
lh-temporalpole	3.229	4.178	4.07	4.151	4.199	4.08
lh-transversetemporal	1.699	2.691	2.63	2.605	2.577	2.509
lh-insula	1.19	2.281	1.969	2.162	2.143	2.11
rh-bankssts	1.176	2.238	2.225	2.203	2.225	2.195
rh-caudalanteriorcingulate	1.243	1.533	1.433	1.513	1.531	1.518
rh-caudalmiddlefrontal	1.618	2.343	2.286	2.187	2.171	2.056
rh-cuneus	1.672	2.562	2.447	2.615	2.574	2.591
rh-entorhinal	2.016	4.323	3.679	4.179	4.182	4.056
rh-fusiform	1.529	2.489	2.395	2.554	2.498	2.358
rh-inferiorparietal	1.396	2.368	2.267	2.375	2.335	2.233
rh-inferiortemporal	2.091	3.077	2.893	3.097	3.088	2.86
rh-isthmuscingulate	1.382	2.464	2.225	2.406	2.395	2.343
rh-lateraloccipital	1.898	2.731	2.592	2.689	2.703	2.497
rh-lateralorbitofrontal	2.328	3.494	3.44	3.336	3.455	3.438
rh-lingual	1.502	2.675	2.486	2.561	2.532	2.53
rh-medialorbitofrontal	2.563	5.088	4.617	4.8	5.024	4.521
rh-middletemporal	1.734	2.838	2.666	2.865	2.824	2.69
rh-parahippocampal	1.021	2.563	2.514	2.459	2.464	2.378
rh-paracentral	2.357	2.267	2.177	2.442	2.391	2.384
rh-parsopercularis	1.496	1.953	1.763	1.925	1.882	1.948
rh-parsorbitalis	2.54	3.588	3.174	3.536	3.51	3.391
rh-parstriangularis	2.051	3.026	2.926	2.878	2.912	2.919
rh-pericalcarine	1.567	2.331	2.2	2.268	2.266	2.278
rh-postcentral	1.322	1.741	1.682	1.663	1.61	1.492
rh-posteriorcingulate	1.33	1.885	1.836	1.715	1.732	1.681
rh-precentral	1.43	1.912	1.898	1.863	1.8	1.692
rh-precuneus	1.337	1.756	1.705	1.788	1.798	1.807
rh-rostralanteriorcingulate	1.391	2.282	2.007	2.188	2.159	2.056
rh-rostralmiddlefrontal	1.846	2.832	2.619	2.715	2.7	2.651
rh-superiorfrontal	1.31	1.802	1.87	1.752	1.735	1.671
rh-superiorparietal	1.504	2.538	2.417	2.488	2.458	2.385
rh-superiortemporal	1.392	1.881	1.818	1.937	1.841	1.821
rh-supramarginal	1.241	2.067	1.977	2.061	1.98	1.925
rh-frontalpole	3.222	7.201	6.628	6.965	7.015	6.211
rh-temporalpole	2.607	3.797	3.201	4.099	3.99	3.87
rh-transversetemporal	1.846	2.774	2.636	2.746	2.664	2.675
rh-insula	1.198	1.82	1.758	1.834	1.826	1.751

Table S7: Coefficient of variation (%) for AD estimation via no denoising (RAW), P2S, BM4D, MPPCA, and SWIN for gray matter cortical regions in HCP test-retest data. Best results are **bolded**.

Cortical Regions	GT	RAW	P2S	MPPCA	BM4D	SWIN
lh-bankssts	1.121	1.997	1.934	2.172	1.976	1.887
lh-caudalanteriorcingulate	1.653	1.933	2.078	2.113	2.063	2.12
lh-caudalmiddlefrontal	1.31	2.219	2.304	2.233	2.15	2.003
lh-cuneus	1.311	1.914	2.043	1.831	1.834	1.8
lh-entorhinal	2.502	3.704	3.95	4.159	3.93	3.935
lh-fusiform	0.9601	1.765	1.694	1.812	1.766	1.551
lh-inferiorparietal	1.37	2.196	2.191	2.1	2.164	1.994
lh-inferiortemporal	1.196	2.824	2.678	3.285	2.936	2.686
lh-isthmuscingulate	1.241	2.249	2.38	1.989	2.067	2.104
lh-lateraloccipital	1.449	2.431	2.506	2.573	2.563	2.366
lh-lateralorbitofrontal	1.785	2.67	3.137	3.296	3.023	2.773
lh-lingual	1.423	1.868	1.826	1.78	1.81	1.729
lh-medialorbitofrontal	2.699	4.136	4.41	4.903	4.557	4.186
lh-middletemporal	1.286	2.208	2.248	2.253	2.179	2.113
lh-parahippocampal	0.965	2.612	2.526	2.525	2.505	2.469
lh-paracentral	1.597	2.459	2.356	2.235	2.262	2.043
lh-parsopercularis	1.348	1.954	1.888	1.877	1.831	1.736
lh-parsorbitalis	1.724	3.114	2.949	3.143	3.131	2.864
lh-parstriangularis	1.658	2.025	2.017	2.037	2.008	1.879
lh-pericalcarine	1.305	2.199	2.149	2.119	2.077	1.987
lh-postcentral	1.491	2.12	2.138	2.118	2.042	2.01
lh-posteriorcingulate	1.272	1.652	1.882	2.098	1.928	1.755
lh-precentral	1.265	1.913	2.038	1.887	1.874	1.763
lh-precuneus	1.092	1.957	1.826	1.774	1.776	1.7
lh-rostralanteriorcingulate	1.779	2.468	2.617	2.431	2.428	2.404
lh-rostralmiddlefrontal	1.715	2.239	2.138	2.355	2.229	2.006
lh-superiorfrontal	1.41	1.834	1.874	1.87	1.774	1.611
lh-superiorparietal	1.417	2.306	2.303	2.151	2.192	2.012
lh-superiortemporal	1.045	2.066	2.042	1.952	1.959	1.874
lh-supramarginal	1.183	1.921	1.85	1.823	1.834	1.789
lh-frontalpole	4.156	6.732	7.093	7.376	6.966	6.481
lh-temporalpole	3.138	4.148	3.804	4.205	4.018	3.921
lh-transversetemporal	1.496	2.677	2.524	2.762	2.621	2.55
lh-insula	0.9875	1.8	1.927	1.749	1.749	1.692
rh-bankssts	1.085	2.234	2.165	2.265	2.179	2.061
rh-caudalanteriorcingulate	1.21	1.582	1.52	1.76	1.589	1.515
rh-caudalmiddlefrontal	1.541	2.19	2.057	2.242	2.072	1.922
rh-cuneus	1.227	2.356	2.464	2.223	2.196	2.162
rh-entorhinal	1.947	2.926	3.426	3.349	3.156	3.04
rh-fusiform	1.407	2.201	2.111	2.284	2.184	1.972

rh-inferiorparietal	1.293	2.344	2.145	2.263	2.19	2.058
rh-inferiortemporal	1.838	2.491	2.669	2.792	2.652	2.339
rh-isthmuscingulate	0.9587	1.833	1.991	1.979	1.837	1.76
rh-lateraloccipital	1.694	2.729	2.328	2.734	2.619	2.38
rh-lateralorbitofrontal	2.252	3.034	2.986	3.5	3.303	3.132
rh-lingual	1.265	2.227	2.281	2.355	2.253	2.089
rh-medialorbitofrontal	2.469	3.872	4.474	4.794	4.419	3.886
rh-middletemporal	1.519	2.523	2.489	2.499	2.472	2.323
rh-parahippocampal	0.8749	2.146	2.098	2.283	2.104	1.94
rh-paracentral	1.513	2.445	2.243	1.936	2.107	1.832
rh-parsopercularis	1.505	1.948	1.864	1.95	1.859	1.816
rh-parsorbitalis	2.468	3.47	3.094	3.688	3.603	3.237
rh-parstriangularis	2.125	2.968	2.772	3.083	2.901	2.883
rh-pericalcarine	1.386	2.054	2.073	2.07	1.972	1.935
rh-postcentral	1.375	1.759	1.558	1.698	1.615	1.528
rh-posteriorcingulate	1.045	1.567	1.629	1.872	1.683	1.532
rh-precentral	1.373	1.985	1.898	1.867	1.84	1.676
rh-precuneus	1.041	1.76	1.718	1.739	1.652	1.57
rh-rostralanteriorcingulate	1.583	1.938	1.954	1.921	1.81	1.659
rh-rostralmiddlefrontal	2.109	2.76	2.501	2.742	2.626	2.598
rh-superiorfrontal	1.444	2.171	2.037	2.08	1.98	1.72
rh-superiorparietal	1.338	2.217	2.292	2.225	2.157	2.059
rh-superiortemporal	1.361	1.897	1.72	1.868	1.76	1.731
rh-supramarginal	1.216	1.91	1.856	1.968	1.861	1.785
rh-frontalpole	3.328	5.482	5.925	6.206	5.899	5.334
rh-temporalpole	2.529	2.799	2.869	3.077	2.812	2.703
rh-transversetemporal	1.616	2.638	2.503	2.871	2.512	2.525
rh-insula	1.071	1.635	1.632	1.554	1.565	1.546

Table S8: Coefficient of variation (%) for FA estimation via no denoising (RAW), P2S, BM4D, MPPCA, and SWIN for white matter regions in HCP test-retest data. Best results are **bolded**.

White Matter Regions	GT	RAW	P2S	MPPCA	BM4D	SWIN
MCP	0.8846	1.758	5.121	2.407	2.195	2.154
PCT	1.274	2.487	5.15	3.657	3.459	3.59
GCC	0.5437	1.189	4.451	1.507	1.393	1.466
BCC	0.6061	1.857	6.761	1.903	1.918	1.964
SCC	0.549	1.441	7.807	1.638	1.671	1.769
FX	1.508	2.783	8.903	3.637	3.267	3.157
CST-R	1.583	2.872	8.514	3.982	3.986	4.075
CST-L	1.221	2.093	7.521	2.796	2.616	2.536
ML-R	1.015	2.223	8.401	2.695	2.487	2.613
ML-L	1.089	2.304	8.228	2.83	2.805	2.586

ICP-R	1.18	2.14	9.024	2.88	2.645	2.612
ICP-L	1.206	2.505	8.379	2.804	2.832	2.668
SCP-R	1.268	2.496	9.602	3.081	3.021	3.161
SCP-L	1.28	2.665	8.458	2.993	2.926	3.114
CP-R	0.7031	1.729	9.776	2.145	2.065	2.025
CP-L	0.6827	2.354	8.168	2.672	2.604	2.705
ALIC-R	1.435	2.825	7.687	3.627	3.271	3.359
ALIC-L	1.125	3.037	7.275	3.428	3.364	3.325
PLIC-R	0.9096	1.654	6.827	1.861	1.861	1.851
PLIC-L	0.9	2.276	7.927	2.605	2.468	2.581
RLIC-R	1.208	2.01	6.992	2.481	2.332	2.318
RLIC-L	1.088	2.651	8.37	3.128	3.006	3.36
ACR-R	1.079	1.425	5.824	2.207	1.925	1.842
ACR-L	0.7943	2.11	5.782	1.887	1.852	1.694
SCR-R	0.9877	1.884	5.467	2.328	2.2	2.187
SCR-L	1.548	5.075	7.557	5.052	4.995	4.893
PCR-R	0.7091	2.143	5.307	2.168	2.097	2.313
PCR-L	1.062	3.229	7.392	2.999	3.141	3.123
PTR-R	0.8196	1.954	8.01	2.189	2.173	2.152
PTR-L	0.9864	2.816	7.782	2.882	2.913	2.763
SS-R	1.096	1.824	8.008	2.107	1.939	2.031
SS-L	1.256	3.011	8.307	3.605	3.301	3.428
EC-R	1.087	1.725	6.079	2.411	2.146	2.204
EC-L	0.7778	1.915	5.476	1.793	1.656	1.724
CGC-R	1.606	2.1	5.282	2.87	2.569	2.509
CGC-L	1.427	3.36	7.266	3.516	3.424	3.223
CGH-R	1.542	3.523	8.564	5.393	4.313	4.564
CGH-L	2.303	3.735	8.204	5.637	4.42	4.656
FXST-R	1.418	2.069	8.61	2.857	2.727	2.781
FXST-L	1.492	2.769	6.629	3.342	3.198	3.359
SLF-R	0.8572	2.1	4.789	2.467	2.329	2.569
SLF-L	0.9807	2.952	6.985	2.973	2.948	2.845
SFO-R	1.743	3.602	9.083	5.006	4.908	4.427
SFO-L	2.151	4.429	8.205	4.484	4.463	4.095
UNC-R	2.527	3.879	9.825	5.056	4.494	4.649
UNC-L	1.687	3.675	8.63	4.451	3.726	3.834
TPT-R	1.335	3.155	7.296	3.2	3.121	3.115
TPT-L	1.465	5.129	9.922	4.702	4.621	4.283

Table S9: Coefficient of variation (%) for MD estimation via no denoising (RAW), P2S, BM4D, MPPCA, and SWIN for white matter regions in HCP test-retest data. Best results are **bolded**.

White Matter Regions	GT	RAW	P2S	MPPCA	BM4D	SWIN

MCP	1.115	2.468	2.793	2.456	2.493	2.333
PCT	1.305	2.788	3.054	2.645	2.682	2.468
GCC	2.778	2.009	2.93	2.213	2.202	2.177
BCC	1.72	2.435	3.093	2.617	2.622	2.457
SCC	1.683	2.268	3.598	2.533	2.527	2.573
FX	3.043	3.625	3.94	3.715	3.565	3.491
CST-R	1.183	2.555	3.085	2.529	2.527	2.473
CST-L	1.324	2.435	3.06	2.45	2.475	2.317
ML-R	1.192	2.478	2.75	2.378	2.397	2.4
ML-L	1.2	2.95	3.223	2.995	2.92	2.773
ICP-R	1.136	2.932	3.292	2.869	2.886	2.717
ICP-L	1.129	2.989	3.172	2.989	3.021	2.825
SCP-R	1.239	2.35	3.406	2.341	2.28	2.322
SCP-L	1.314	3.216	4.072	3.196	3.157	3.165
CP-R	1.563	2.487	3.991	2.693	2.703	2.707
CP-L	2.101	3.488	4.297	3.542	3.609	3.758
ALIC-R	1.833	2.394	3.271	2.576	2.464	2.411
ALIC-L	3.329	4.885	5.901	5.357	5.158	5.135
PLIC-R	0.9723	1.688	2.429	1.745	1.745	1.672
PLIC-L	2.127	3.626	4.358	3.706	3.728	3.753
RLIC-R	1.55	2.747	3.091	2.72	2.76	2.69
RLIC-L	2.075	2.738	2.711	2.824	2.803	2.616
ACR-R	1.584	1.891	2.167	1.889	1.861	1.795
ACR-L	2.51	2.562	2.812	2.632	2.583	2.57
SCR-R	1.396	2.543	2.902	2.464	2.545	2.514
SCR-L	2.799	4.603	4.659	4.642	4.646	4.464
PCR-R	0.9936	2.098	2.158	2.065	2.054	2.035
PCR-L	2.202	3.795	4.016	3.864	3.752	3.486
PTR-R	1.454	2.691	3.608	2.676	2.678	2.629
PTR-L	2.067	3.087	3.658	3.151	3.13	2.928
SS-R	2.316	3.026	3.678	3.063	3.03	2.867
SS-L	2.248	2.598	2.715	2.662	2.663	2.759
EC-R	1.298	2.444	2.821	2.462	2.434	2.288
EC-L	1.598	1.961	2.075	1.988	1.949	1.906
CGC-R	1.382	1.879	2.291	1.85	1.836	1.703
CGC-L	3.309	4.649	5.186	4.923	4.796	4.582
CGH-R	1.198	2.548	3.019	2.545	2.414	2.359
CGH-L	1.625	2.832	2.867	2.778	2.831	2.772
FXST-R	1.427	2.418	3.031	2.475	2.313	2.376
FXST-L	1.934	2.497	2.94	2.651	2.508	2.656
SLF-R	1.305	2.274	2.493	2.282	2.287	2.27
SLF-L	2.445	4.384	4.611	4.495	4.441	4.152
SFO-R	2.321	3.569	4.03	3.282	3.345	3.34
SFO-L	4.599	6.482	6.575	6.087	6.358	5.989
UNC-R	1.902	3.472	3.306	3.35	3.432	3.134

UNC-L	1.434	2.748	3.065	2.785	2.643	2.328
TPT-R	1.822	3.362	3.212	3.335	3.281	3.523
TPT-L	2.647	5.352	5.179	5.17	4.859	4.607

Table S10: Coefficient of variation (%) for RD estimation via no denoising (RAW), P2S, BM4D, MPPCA, and SWIN for white matter regions in HCP test-retest data. Best results are **bolded**.

White Matter Regions	GT	RAW	P2S	MPPCA	BM4D	SWIN
MCP	1.777	3.89	3.39	3.866	3.878	3.608
PCT	1.843	4.329	3.462	4.174	4.22	3.843
GCC	2.688	4.209	3.269	4.431	4.415	4.289
BCC	3.027	6.325	4.038	6.256	6.47	5.827
SCC	3.396	6.538	4.377	7.04	7.265	7.21
FX	5.346	6.488	4.07	6.619	6.684	6.392
CST-R	2.075	4.493	3.807	4.565	4.457	4.307
CST-L	2.263	3.823	3.751	3.783	3.729	3.386
ML-R	1.871	4.188	3.476	4.223	4.108	4.002
ML-L	2.231	4.896	3.956	4.768	4.756	4.303
ICP-R	1.745	4.517	3.773	4.687	4.626	4.271
ICP-L	1.684	4.9	3.738	4.789	4.76	4.306
SCP-R	2.758	4.367	4.609	4.411	4.233	4.167
SCP-L	3.269	5.961	4.919	5.88	5.788	5.788
CP-R	2.61	6.292	5.319	6.69	6.774	6.444
CP-L	3.464	7.232	5.223	7.151	7.39	7.548
ALIC-R	2.994	5.366	4.228	5.251	5.155	5.0
ALIC-L	4.463	8.576	6.735	8.487	8.472	8.228
PLIC-R	2.305	3.811	2.997	3.653	3.723	3.596
PLIC-L	3.474	7.072	4.838	6.901	6.935	6.717
RLIC-R	2.426	4.542	3.333	4.326	4.404	4.185
RLIC-L	2.987	4.997	3.246	4.721	4.86	4.915
ACR-R	1.691	2.569	2.459	2.448	2.486	2.224
ACR-L	2.281	3.736	3.135	3.218	3.299	3.122
SCR-R	1.88	3.446	2.955	3.407	3.435	3.325
SCR-L	3.617	7.646	5.211	7.09	7.162	6.627
PCR-R	1.245	2.995	2.19	2.834	2.773	2.77
PCR-L	2.585	5.717	4.662	5.296	5.275	4.829
PTR-R	2.027	4.867	4.293	4.853	4.811	4.491
PTR-L	3.28	6.902	4.41	6.631	6.653	5.997
SS-R	3.136	4.241	4.235	4.211	4.153	3.819
SS-L	3.456	5.32	3.19	5.222	5.104	5.115
EC-R	1.623	3.248	3.321	3.067	3.084	2.767
EC-L	1.887	3.033	2.406	2.703	2.728	2.672
CGC-R	2.754	3.682	2.631	3.57	3.407	2.868

CGC-L	5.231	8.127	5.898	7.777	7.876	6.926
CGH-R	2.048	5.438	3.64	5.73	5.296	4.947
CGH-L	3.226	6.181	3.55	6.105	6.12	5.991
FXST-R	2.657	4.157	3.741	4.341	4.063	4.15
FXST-L	3.382	5.425	3.347	5.139	5.044	5.269
SLF-R	1.964	3.701	2.711	3.774	3.741	3.648
SLF-L	3.091	6.39	5.116	5.97	5.988	5.318
SFO-R	3.287	5.503	4.388	5.154	5.249	4.969
SFO-L	5.448	8.469	7.166	7.28	7.704	7.048
UNC-R	3.389	5.169	3.83	5.121	5.101	4.596
UNC-L	2.135	4.589	3.704	4.316	4.249	3.716
TPT-R	2.797	5.378	3.545	5.115	4.902	4.959
TPT-L	4.517	10.36	6.169	9.479	9.101	8.125

Table S11: Coefficient of variation (%) for AD estimation via no denoising (RAW), P2S, BM4D, MPPCA, and SWIN for white matter regions in HCP test-retest data. Best results are **bolded**.

White Matter Regions	GT	RAW	P2S	MPPCA	BM4D	SWIN
MCP	0.9666	1.73	2.251	1.65	1.684	1.58
PCT	1.277	2.307	2.614	2.047	2.024	1.865
GCC	2.995	1.74	2.762	2.047	1.9	1.909
BCC	1.52	1.627	2.767	1.74	1.663	1.678
SCC	1.347	1.386	3.033	1.381	1.385	1.381
FX	2.441	3.258	3.824	3.366	3.061	2.969
CST-R	1.572	2.09	2.583	2.121	2.048	1.91
CST-L	1.254	2.277	2.572	2.225	2.161	2.001
ML-R	1.316	2.433	2.625	2.227	2.195	2.132
ML-L	1.099	2.586	2.833	2.755	2.544	2.305
ICP-R	1.305	2.467	2.728	2.246	2.216	2.042
ICP-L	1.313	2.685	2.845	2.484	2.561	2.271
SCP-R	1.445	2.053	2.959	2.165	2.105	2.157
SCP-L	1.264	2.605	3.584	2.664	2.591	2.565
CP-R	1.52	2.264	2.751	2.302	2.259	2.252
CP-L	1.718	2.847	3.487	2.819	2.8	2.673
ALIC-R	1.588	1.85	2.695	2.208	2.008	2.04
ALIC-L	2.83	3.5	4.992	3.992	3.678	3.613
PLIC-R	0.7791	1.408	2.29	1.404	1.407	1.372
PLIC-L	1.676	2.519	3.912	2.414	2.468	2.422
RLIC-R	1.642	2.108	2.91	2.158	2.12	2.057
RLIC-L	1.788	1.74	2.772	1.906	1.8	1.659
ACR-R	1.779	1.731	2.118	1.822	1.754	1.693
ACR-L	2.723	1.986	2.662	2.36	2.212	2.219
SCR-R	1.169	2.219	2.855	2.009	2.069	2.063

SCR-L	2.231	2.431	3.858	2.77	2.688	2.656
PCR-R	0.9502	1.741	2.194	1.73	1.692	1.666
PCR-L	1.968	2.654	3.238	2.844	2.707	2.558
PTR-R	1.431	1.948	2.856	1.917	1.933	1.919
PTR-L	1.754	1.85	3.071	1.867	1.86	1.719
SS-R	2.224	2.712	3.024	2.876	2.798	2.741
SS-L	1.799	1.881	2.47	2.095	1.94	1.843
EC-R	1.399	2.094	2.303	2.283	2.175	2.103
EC-L	1.49	1.586	1.99	1.794	1.695	1.627
CGC-R	1.594	1.918	2.293	2.058	2.103	1.915
CGC-L	2.785	3.325	4.139	3.772	3.643	3.587
CGH-R	1.642	3.174	2.669	3.538	2.915	3.008
CGH-L	1.858	2.564	2.75	2.927	2.585	2.349
FXST-R	1.744	2.245	2.352	2.512	2.411	2.298
FXST-L	1.668	1.999	2.526	2.314	2.115	2.063
SLF-R	1.165	1.668	2.243	1.671	1.693	1.677
SLF-L	2.151	3.199	3.882	3.594	3.502	3.368
SFO-R	1.93	2.858	3.737	2.773	2.717	2.581
SFO-L	4.139	5.298	5.767	5.61	5.57	5.314
UNC-R	1.792	2.965	3.445	2.916	2.922	2.817
UNC-L	1.646	3.124	2.891	3.263	3.014	2.848
TPT-R	1.721	2.927	3.331	2.888	2.979	2.94
TPT-L	2.405	5.428	4.492	4.707	4.251	3.832

Table S12: Coefficient of variation (%) for NDI estimation via no denoising (RAW), P2S, BM4D, MPPCA, and SWIN for gray matter cortical regions in HCP test-retest data. Best results are **bolded**.

Cortical Regions	RAW	P2S	MPPCA	BM4D	SWIN
lh-bankssts	4.446	4.584	4.447	4.535	1.515
lh-caudalanteriorcingulate	5.382	5.504	5.378	5.56	2.84
lh-caudalmiddlefrontal	4.747	4.848	4.746	4.79	2.041
lh-cuneus	4.533	4.605	4.532	4.561	2.044
lh-entorhinal	5.223	5.491	5.224	5.372	3.385
lh-fusiform	4.042	4.234	4.044	4.012	1.475
lh-inferiorparietal	5.157	5.151	5.156	5.244	2.358
lh-inferiortemporal	4.396	4.599	4.4	4.503	2.0
lh-isthmuscingulate	4.489	4.641	4.486	4.577	2.263
lh-lateraloccipital	4.753	4.774	4.745	4.748	2.273
lh-lateralorbitofrontal	4.031	4.211	4.031	4.141	2.293
lh-lingual	4.372	4.501	4.372	4.434	2.126
lh-medialorbitofrontal	4.627	4.883	4.629	4.798	3.064
lh-middletemporal	5.06	5.265	5.06	5.174	2.189
lh-parahippocampal	4.564	4.754	4.564	4.689	2.094

lh-paracentral	5.069	5.229	5.069	5.115	2.376
lh-parsopercularis	5.303	5.443	5.302	5.267	2.585
lh-parsorbitalis	5.418	5.507	5.424	5.481	3.185
lh-parstriangularis	5.575	5.709	5.577	5.521	2.88
lh-pericalcarine	4.302	4.538	4.301	4.417	1.686
lh-postcentral	4.673	4.82	4.672	4.611	1.989
lh-posteriorcingulate	4.448	4.694	4.446	4.42	1.525
lh-precentral	4.227	4.379	4.227	4.183	1.626
lh-precuneus	4.317	4.422	4.317	4.41	1.483
lh-rostralanteriorcingulate	5.784	5.874	5.781	6.086	3.603
lh-rostralmiddlefrontal	5.911	6.001	5.911	5.762	3.483
lh-superiorfrontal	5.729	5.814	5.729	5.604	3.173
lh-superiorparietal	4.95	4.934	4.949	4.973	2.124
lh-superiortemporal	4.41	4.543	4.41	4.538	1.777
lh-supramarginal	4.698	4.799	4.697	4.691	1.855
lh-frontalpole	7.348	7.478	7.349	7.381	6.353
lh-temporalpole	7.0	7.17	7.005	7.116	5.154
lh-transversetemporal	4.717	4.967	4.717	4.797	2.222
lh-insula	4.294	4.47	4.293	4.352	1.646
rh-bankssts	4.546	4.598	4.548	4.645	1.639
rh-caudalanteriorcingulate	4.877	5.033	4.871	4.99	2.289
rh-caudalmiddlefrontal	5.39	5.54	5.39	5.4	2.768
rh-cuneus	4.158	4.217	4.16	4.152	1.513
rh-entorhinal	4.614	4.858	4.613	4.872	2.556
rh-fusiform	4.245	4.508	4.253	4.321	1.766
rh-inferiorparietal	5.872	5.862	5.873	6.017	2.965
rh-inferiortemporal	4.673	4.863	4.665	4.78	2.499
rh-isthmuscingulate	3.865	4.023	3.863	3.973	1.573
rh-lateraloccipital	4.875	4.951	4.873	4.911	2.441
rh-lateralorbitofrontal	4.014	4.165	4.014	4.096	2.271
rh-lingual	4.066	4.234	4.066	4.144	1.859
rh-medialorbitofrontal	4.602	4.731	4.604	4.738	3.058
rh-middletemporal	5.63	5.738	5.63	5.72	2.681
rh-parahippocampal	3.981	4.178	3.979	4.186	1.665
rh-paracentral	4.842	4.912	4.843	4.911	2.075
rh-parsopercularis	5.778	5.789	5.776	5.885	2.967
rh-parsorbitalis	5.631	5.63	5.634	5.727	3.536
rh-parstriangularis	6.237	6.305	6.236	6.238	3.567
rh-pericalcarine	4.166	4.164	4.165	4.144	1.584
rh-postcentral	4.792	4.925	4.791	4.801	2.159
rh-posteriorcingulate	4.322	4.481	4.323	4.4	1.363
rh-precentral	4.968	5.027	4.968	4.95	2.346
rh-precuneus	4.275	4.386	4.274	4.309	1.487
rh-rostralanteriorcingulate	5.218	5.352	5.221	5.36	2.992
rh-rostralmiddlefrontal	6.232	6.35	6.232	6.247	3.743

rh-superiorfrontal	5.542	5.643	5.542	5.451	3.038
rh-superiorparietal	4.914	4.912	4.915	4.974	2.078
rh-superiortemporal	5.326	5.391	5.325	5.432	2.539
rh-supramarginal	5.349	5.354	5.349	5.48	2.508
rh-frontalpole	6.226	6.288	6.229	6.331	5.004
rh-temporalpole	6.107	6.279	6.112	6.309	4.05
rh-transversetemporal	4.248	4.383	4.25	4.392	2.006
rh-insula	4.567	4.686	4.562	4.655	1.863

Table S13: Coefficient of variation (%) for ODI estimation via no denoising (RAW), P2S, BM4D, MPPCA, and SWIN for gray matter cortical regions in HCP test-retest data. Best results are **bolded**.

Cortical Regions	RAW	P2S	MPPCA	BM4D	SWIN
lh-bankssts	1.456	1.435	1.459	1.561	1.218
lh-caudalanteriorcingulate	1.894	1.931	1.897	2.087	1.875
lh-caudalmiddlefrontal	2.444	2.436	2.446	2.651	2.44
lh-cuneus	1.393	1.381	1.393	1.579	1.286
lh-entorhinal	1.61	1.622	1.624	1.801	1.585
lh-fusiform	1.156	1.175	1.152	1.226	0.9686
lh-inferiorparietal	1.503	1.486	1.503	1.599	1.201
lh-inferiortemporal	1.514	1.518	1.514	1.627	1.292
lh-isthmuscingulate	1.433	1.382	1.432	1.675	1.555
lh-lateraloccipital	1.327	1.375	1.331	1.556	1.288
lh-lateralorbitofrontal	1.391	1.343	1.381	1.57	1.492
lh-lingual	0.9848	0.9468	0.9772	1.184	0.9448
lh-medialorbitofrontal	1.629	1.638	1.594	1.892	1.73
lh-middletemporal	1.6	1.613	1.6	1.743	1.391
lh-parahippocampal	1.638	1.583	1.645	1.712	1.398
lh-paracentral	1.383	1.37	1.384	1.564	1.546
lh-parsopercularis	2.046	2.064	2.048	2.306	2.174
lh-parsorbitalis	2.042	2.007	2.051	2.165	2.178
lh-parstriangularis	2.61	2.574	2.617	2.858	2.743
lh-pericalcarine	1.554	1.516	1.551	1.668	1.562
lh-postcentral	1.338	1.34	1.335	1.495	1.421
lh-posteriorcingulate	1.095	1.104	1.091	1.217	1.068
lh-precentral	1.671	1.687	1.676	1.874	1.782
lh-precuneus	1.052	1.08	1.053	1.242	1.013
lh-rostralanteriorcingulate	2.035	2.053	2.044	2.447	2.388
lh-rostralmiddlefrontal	3.188	3.158	3.194	3.48	3.481
lh-superiorfrontal	2.373	2.365	2.373	2.615	2.568
lh-superiorparietal	1.847	1.814	1.848	1.956	1.636
lh-superiortemporal	1.419	1.431	1.42	1.465	1.23
lh-supramarginal	1.417	1.437	1.419	1.542	1.309

lh-frontalpole	3.573	3.492	3.587	3.986	3.907
lh-temporalpole	2.376	2.404	2.415	2.693	2.357
lh-transversetemporal	1.075	1.135	1.071	1.269	1.08
lh-insula	1.848	1.877	1.861	1.923	1.798
rh-bankssts	1.439	1.428	1.438	1.575	1.324
rh-caudalanteriorcingulate	2.74	2.704	2.755	3.085	2.784
rh-caudalmiddlefrontal	2.134	2.115	2.133	2.326	2.107
rh-cuneus	1.533	1.489	1.536	1.575	1.575
rh-entorhinal	1.513	1.46	1.527	1.705	1.364
rh-fusiform	0.9599	0.9971	0.9683	1.08	0.9813
rh-inferiorparietal	1.266	1.296	1.266	1.313	1.118
rh-inferiortemporal	1.185	1.227	1.203	1.391	1.256
rh-isthmuscingulate	1.842	1.799	1.851	1.948	1.767
rh-lateraloccipital	1.084	1.106	1.085	1.242	1.137
rh-lateralorbitofrontal	1.293	1.282	1.275	1.557	1.442
rh-lingual	1.326	1.324	1.332	1.486	1.348
rh-medialorbitofrontal	1.497	1.455	1.582	1.966	1.836
rh-middletemporal	1.948	1.95	1.942	2.132	1.806
rh-parahippocampal	1.194	1.113	1.196	1.214	1.155
rh-paracentral	2.096	2.112	2.097	2.299	2.204
rh-parsopercularis	2.25	2.238	2.256	2.549	2.264
rh-parsorbitalis	2.625	2.624	2.622	3.03	2.718
rh-parstriangularis	3.084	3.078	3.076	3.486	3.13
rh-pericalcarine	1.342	1.291	1.346	1.608	1.477
rh-postcentral	1.463	1.489	1.464	1.659	1.527
rh-posteriorcingulate	2.026	1.996	2.027	2.258	2.037
rh-precentral	1.692	1.689	1.69	1.831	1.714
rh-precuneus	1.609	1.588	1.611	1.619	1.49
rh-rostralanteriorcingulate	2.596	2.605	2.615	2.984	2.936
rh-rostralmiddlefrontal	3.121	3.084	3.124	3.512	3.17
rh-superiorfrontal	2.776	2.771	2.778	3.066	2.927
rh-superiorparietal	1.175	1.242	1.175	1.334	1.208
rh-superiortemporal	1.671	1.677	1.665	1.896	1.588
rh-supramarginal	1.399	1.446	1.4	1.488	1.253
rh-frontalpole	2.726	2.707	2.712	3.12	3.005
rh-temporalpole	2.084	2.117	2.154	2.544	2.156
rh-transversetemporal	1.567	1.552	1.567	1.891	1.661
rh-insula	1.566	1.543	1.566	1.77	1.481

Table S14: Coefficient of variation (%) for FISO estimation via no denoising (RAW), P2S, BM4D, MPPCA, and SWIN for gray matter cortical regions in HCP test-retest data. Best results are **bolded**.

Cortical Regions	RAW	P2S	MPPCA	BM4D	SWIN
lh-bankssts	20.25	20.62	20.26	22.03	16.25
lh-caudalanteriorcingulate	16.0	15.88	15.99	16.66	14.27
lh-caudalmiddlefrontal	15.85	16.57	15.86	16.71	12.2
lh-cuneus	12.74	13.56	12.74	13.57	9.165
lh-entorhinal	13.39	13.91	13.39	13.88	10.67
lh-fusiform	15.35	16.14	15.35	16.23	10.5
lh-inferiorparietal	14.08	14.7	14.09	15.04	10.32
lh-inferiortemporal	17.69	18.86	17.69	18.62	13.32
lh-isthmuscingulate	11.52	12.06	11.52	12.05	9.708
lh-lateraloccipital	11.84	12.4	11.84	12.08	6.857
lh-lateralorbitofrontal	11.94	13.39	11.94	12.86	8.725
lh-lingual	9.904	10.48	9.905	10.36	6.796
lh-medialorbitofrontal	13.97	14.12	13.97	14.94	11.49
lh-middletemporal	17.8	17.49	17.81	18.85	13.93
lh-parahippocampal	14.86	15.2	14.86	15.54	10.94
lh-paracentral	15.14	15.31	15.14	15.55	10.45
lh-parsopercularis	15.18	15.57	15.19	16.31	11.26
lh-parsorbitalis	17.53	17.62	17.53	19.02	13.48
lh-parstriangularis	17.03	17.19	17.03	18.7	13.15
lh-pericalcarine	12.32	13.36	12.31	13.33	8.79
lh-postcentral	13.57	13.87	13.57	14.16	9.935
lh-posteriorcingulate	13.8	14.19	13.79	14.74	9.548
lh-precentral	14.45	14.91	14.45	15.08	10.56
lh-precuneus	14.64	15.21	14.64	15.18	9.929
lh-rostralanteriorcingulate	15.69	16.16	15.7	16.46	12.45
lh-rostralmiddlefrontal	14.31	14.3	14.31	14.89	10.59
lh-superiorfrontal	13.24	13.78	13.23	13.42	9.182
lh-superiorparietal	14.43	15.14	14.43	14.68	9.181
lh-superiortemporal	11.94	12.29	11.95	12.1	7.953
lh-supramarginal	15.02	15.2	15.02	15.65	10.54
lh-frontalpole	14.73	14.31	14.74	15.14	12.12
lh-temporalpole	20.92	20.67	20.92	22.12	18.51
lh-transversetemporal	12.84	12.87	12.84	13.42	9.818
lh-insula	14.09	14.23	14.1	15.13	10.31
rh-bankssts	17.14	17.59	17.15	17.86	11.53
rh-caudalanteriorcingulate	15.39	15.8	15.38	16.43	11.81
rh-caudalmiddlefrontal	17.9	18.35	17.9	18.33	12.69
rh-cuneus	13.66	14.18	13.66	14.69	10.41
rh-entorhinal	12.66	13.45	12.67	13.51	9.524
rh-fusiform	15.53	17.02	15.53	16.22	11.71
rh-inferiorparietal	20.28	20.66	20.28	21.22	16.56
rh-inferiortemporal	17.04	18.11	17.04	17.74	13.74
rh-isthmuscingulate	13.85	14.19	13.87	15.09	9.837
rh-lateraloccipital	16.01	16.75	16.0	16.64	12.49

rh-lateralorbitofrontal	13.18	13.91	13.18	14.22	10.8	
rh-lingual	12.02	12.26	12.03	12.63	7.996	
rh-medialorbitofrontal	14.0	14.7	14.01	14.7	10.17	
rh-middletemporal	20.97	20.84	20.96	22.1	17.85	
rh-parahippocampal	14.12	14.35	14.12	14.94	9.904	
rh-paracentral	16.19	16.31	16.19	16.94	11.87	
rh-parsopercularis	14.7	14.71	14.7	15.55	10.51	
rh-parsorbitalis	13.52	12.93	13.52	14.24	12.31	
rh-parstriangularis	16.5	16.46	16.5	17.15	13.15	
rh-pericalcarine	12.98	13.23	12.98	13.78	8.894	
rh-postcentral	12.71	13.27	12.71	13.08	8.309	
rh-posteriorcingulate	16.29	16.5	16.29	17.59	11.32	
rh-precentral	15.58	16.4	15.58	15.89	10.88	
rh-precuneus	14.46	14.78	14.46	15.13	10.06	
rh-rostralanteriorcingulate	15.47	15.37	15.46	15.8	11.04	
rh-rostralmiddlefrontal	15.84	15.72	15.84	16.55	11.49	
rh-superiorfrontal	13.28	13.9	13.28	13.53	9.48	
rh-superiorparietal	15.21	15.76	15.21	15.48	9.97	
rh-superiortemporal	16.04	16.31	16.03	16.7	11.89	
rh-supramarginal	18.14	18.57	18.13	18.79	13.99	
rh-frontalpole	13.36	12.74	13.36	13.82	10.89	
rh-temporalpole	15.42	15.98	15.41	16.28	11.37	
rh-transversetemporal	14.0	14.7	14.01	14.66	11.29	
rh-insula	11.83	11.91	11.84	12.2	8.222	

Table S15: Coefficient of variation (%) for NDI estimation via no denoising (RAW), P2S, BM4D, MPPCA, and SWIN for white matter regions in HCP test-retest data. Best results are **bolded**.

White Matter Regions	RAW	P2S	MPPCA	BM4D	SWIN
MCP	1.515	1.779	1.515	1.581	1.008
PCT	2.165	2.413	2.168	2.454	1.856
GCC	2.297	2.574	2.297	2.461	2.092
BCC	2.411	2.632	2.408	2.41	1.355
SCC	1.662	1.935	1.66	1.663	0.9457
FX	3.456	3.894	3.456	3.618	2.446
CST-R	1.727	2.007	1.728	1.928	1.41
CST-L	1.695	1.975	1.696	1.906	1.313
ML-R	2.806	3.067	2.803	2.915	2.012
ML-L	2.74	3.079	2.742	2.953	1.986
ICP-R	2.492	2.715	2.493	2.44	1.568
ICP-L	2.175	2.4	2.176	2.192	1.213
SCP-R	2.055	2.312	2.053	2.137	1.292
SCP-L	2.101	2.317	2.099	2.271	1.278

CP-R	1.494	1.654	1.492	1.627	1.193
CP-L	1.567	1.708	1.567	1.637	1.166
ALIC-R	1.962	2.357	1.962	2.149	1.29
ALIC-L	2.795	3.181	2.795	3.029	2.27
PLIC-R	1.697	1.926	1.696	1.757	1.058
PLIC-L	2.386	2.575	2.389	2.575	1.844
RLIC-R	2.673	2.928	2.671	2.746	1.789
RLIC-L	2.416	2.737	2.417	2.468	1.508
ACR-R	2.871	3.233	2.874	3.019	2.289
ACR-L	3.576	3.879	3.575	3.685	3.245
SCR-R	2.336	2.615	2.333	2.276	1.434
SCR-L	2.563	2.655	2.561	2.522	1.342
PCR-R	2.463	2.769	2.461	2.421	1.107
PCR-L	2.652	2.753	2.652	2.578	1.205
PTR-R	2.754	3.038	2.75	2.741	1.5
PTR-L	2.74	2.961	2.737	2.819	1.297
SS-R	3.261	3.464	3.263	3.38	2.311
SS-L	2.9	3.141	2.898	2.937	1.813
EC-R	3.198	3.587	3.189	3.265	1.631
EC-L	3.293	3.563	3.284	3.362	1.985
CGC-R	2.458	2.679	2.458	2.581	1.472
CGC-L	2.676	3.017	2.677	2.731	1.678
CGH-R	2.735	3.183	2.73	2.843	1.826
CGH-L	2.928	3.319	2.931	3.131	2.025
FXST-R	2.734	3.012	2.73	2.913	1.8
FXST-L	2.612	2.935	2.608	2.758	1.613
SLF-R	2.215	2.49	2.215	2.154	1.237
SLF-L	2.29	2.477	2.289	2.353	1.227
SFO-R	2.4	2.858	2.392	2.476	1.663
SFO-L	4.2	4.516	4.2	4.327	3.189
UNC-R	4.15	4.42	4.147	4.146	2.478
UNC-L	3.321	3.598	3.326	3.437	1.898
TPT-R	3.138	3.199	3.143	3.21	1.465
TPT-L	3.327	3.476	3.328	3.461	2.015

Table S16: Coefficient of variation (%) for ODI estimation via no denoising (RAW), P2S, BM4D, MPPCA, and SWIN for white matter regions in HCP test-retest data. Best results are **bolded**.

White Matter Regions	RAW	P2S	MPPCA	BM4D	SWIN
MCP	3.362	3.657	3.388	3.313	3.021
PCT	6.411	7.023	6.45	6.495	5.759
GCC	4.48	8.522	4.374	4.372	4.732
BCC	2.954	6.584	2.948	3.064	3.194

SCC	2.629	6.068	2.62	2.708	3.016	
FX	4.123	6.529	4.097	3.882	3.714	
CST-R	5.267	7.198	5.27	5.845	5.718	
CST-L	6.191	8.277	6.199	6.811	6.217	
ML-R	5.546	7.705	5.553	5.584	5.075	
ML-L	4.503	7.564	4.494	4.728	4.665	
ICP-R	4.943	4.548	4.97	4.836	3.78	
ICP-L	4.963	4.89	4.954	5.272	4.088	
SCP-R	4.466	5.366	4.499	4.665	4.013	
SCP-L	3.902	5.28	3.914	4.248	4.151	
CP-R	3.911	5.433	3.901	4.143	4.416	
CP-L	4.836	5.506	4.855	5.681	4.735	
ALIC-R	5.263	9.024	5.267	5.578	5.486	
ALIC-L	6.078	8.724	6.107	6.588	6.101	
PLIC-R	3.888	5.312	3.888	4.088	4.374	
PLIC-L	4.902	5.99	4.888	5.133	4.598	
RLIC-R	5.925	7.585	5.95	6.164	5.933	
RLIC-L	5.959	7.082	6.006	6.329	5.658	
ACR-R	4.905	4.691	5.113	5.115	4.483	
ACR-L	5.189	5.716	5.338	5.384	5.077	
SCR-R	3.897	3.999	3.94	4.041	3.087	
SCR-L	4.123	3.892	4.131	4.213	3.403	
PCR-R	5.427	5.845	5.414	5.454	4.752	
PCR-L	4.327	4.51	4.324	4.448	3.751	
PTR-R	3.826	7.196	3.81	3.832	3.388	
PTR-L	3.607	6.62	3.624	3.528	3.126	
SS-R	5.301	6.409	5.387	5.699	4.462	
SS-L	4.796	7.46	4.807	5.135	4.596	
EC-R	4.632	4.821	4.794	5.079	3.874	
EC-L	5.111	5.141	5.238	5.609	4.201	
CGC-R	6.461	11.34	6.417	5.946	6.844	
CGC-L	4.02	7.941	4.034	4.17	4.294	
CGH-R	6.96	11.87	6.989	8.189	8.631	
CGH-L	8.883	14.75	8.905	11.35	11.26	
FXST-R	7.167	9.159	7.218	7.952	6.859	
FXST-L	5.483	9.262	5.524	6.995	5.909	
SLF-R	4.322	6.852	4.352	4.417	4.234	
SLF-L	4.154	6.107	4.185	4.239	3.653	
SFO-R	6.589	4.726	6.671	6.987	4.415	
SFO-L	7.992	6.05	8.138	8.054	6.105	
UNC-R	10.94	9.57	11.27	11.64	7.213	
UNC-L	9.61	9.845	9.77	9.422	8.762	
TPT-R	6.067	7.771	6.078	5.889	4.38	
TPT-L	8.446	7.238	8.596	7.308	8.824	

Table S17: Coefficient of variation (%) for FISO estimation via no denoising (RAW), P2S, BM4D, MPPCA, and SWIN for white matter regions in HCP test-retest data. Best results are **bolded**.

White Matter Regions	RAW	P2S	MPPCA	BM4D	SWIN
MCP	9.293	11.18	9.293	9.485	8.199
PCT	10.05	11.01	10.05	10.69	9.466
GCC	8.581	9.76	8.595	8.68	7.502
BCC	13.03	14.86	13.04	14.01	11.4
SCC	14.05	15.38	14.04	14.56	13.58
FX	10.7	11.71	10.7	11.24	9.04
CST-R	7.849	9.142	7.858	8.213	7.474
CST-L	7.481	8.844	7.479	7.854	7.359
ML-R	14.83	14.73	14.83	15.57	15.43
ML-L	15.23	15.5	15.24	16.03	15.48
ICP-R	13.72	15.04	13.72	14.3	12.28
ICP-L	12.23	13.42	12.23	12.89	11.13
SCP-R	6.914	7.976	6.916	6.785	6.027
SCP-L	9.039	9.853	9.041	8.903	8.5
CP-R	12.29	12.16	12.29	12.95	12.56
CP-L	11.49	11.24	11.49	11.8	12.57
ALIC-R	11.26	12.56	11.27	11.73	10.45
ALIC-L	27.1	29.05	27.14	30.64	27.98
PLIC-R	7.903	9.073	7.91	8.285	6.797
PLIC-L	22.36	21.75	22.38	24.67	22.52
RLIC-R	12.57	13.76	12.56	13.09	10.55
RLIC-L	16.96	16.85	16.94	17.86	15.65
ACR-R	10.04	9.664	10.06	10.68	8.19
ACR-L	11.13	11.61	11.17	11.95	9.5
SCR-R	18.75	18.7	18.76	19.83	17.05
SCR-L	27.49	25.22	27.52	30.04	27.06
PCR-R	16.25	16.56	16.25	16.88	14.29
PCR-L	24.65	22.98	24.64	26.66	22.13
PTR-R	13.36	14.61	13.35	14.09	11.48
PTR-L	19.24	21.29	19.24	20.65	19.07
SS-R	15.01	15.48	15.02	16.12	13.1
SS-L	13.72	15.49	13.73	14.52	12.85
EC-R	18.27	18.17	18.25	20.9	14.93
EC-L	18.64	19.23	18.65	21.78	16.17
CGC-R	9.315	11.29	9.309	9.842	7.469
CGC-L	16.24	17.55	16.23	16.62	15.79
CGH-R	10.94	11.69	10.93	11.8	8.834
CGH-L	14.5	15.3	14.51	16.55	13.36
FXST-R	10.72	10.82	10.72	11.39	9.431
FXST-L	14.11	14.27	14.11	14.27	12.34

SLF-R	13.89	15.44	13.89	14.49	11.89
SLF-L	28.13	28.38	28.13	30.91	28.06
SFO-R	16.56	16.77	16.53	18.42	17.01
SFO-L	31.93	30.03	31.85	36.08	32.12
UNC-R	32.87	29.24	32.94	40.59	31.43
UNC-L	22.72	21.77	22.79	27.0	17.55
TPT-R	13.09	12.68	13.08	13.26	12.1
TPT-L	29.37	27.04	29.34	28.02	26.44